GPO PRICE $ _____

CFSTI PRICE(S) $ _____

Hard copy (HC) _____

Microfiche (MF) _____

ff 653 July 65

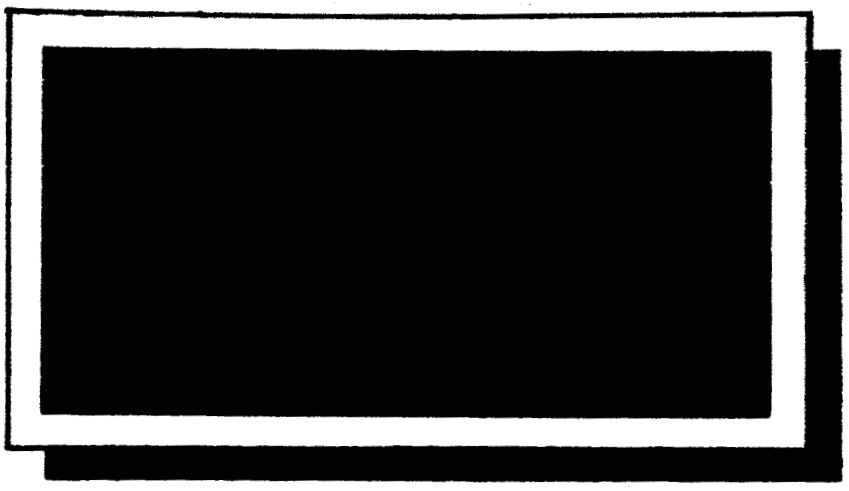

CENTER FOR SPACE RESEARCH

MASSACHUSETTS INSTITUTE OF TECHNOLOGY

EXPERIMENTS ON EKMAN LAYER INSTABILITY

by
Peter R. Tatro

April 1966

CSR-T[redacted]-66-2

MASSACHUSETTS INSTITUTE OF TECHNOLOGY
Center for Space Research

EXPERIMENTS ON EKMAN LAYER INSTABILITY

by

Peter R. Tatro
Department of Meteorology

on

NASA GRANT NsG-496

NATIONAL AERONAUTICS AND SPACE ADMINISTRATION
Office of Grants and Research Contracts

This report was submitted as a thesis to the Department of Meteorology at M.I.T. in partial fulfillment of the requirements for the degree of Doctor of Philosophy.

ABSTRACT

Laboratory measurements were made of the instabilities of the Ekman layer using hot wire anemometers. The apparatus consisted of two parallel circular rotating plates forming a spool; the air was admitted through screens at the outer edge and removed through a screen cage at the hub. In the Ekman layers formed on the inner surfaces of the plates, measurements were made of the mean velocities as functions of r and z; the velocity fluctuations were also measured.

The results show the changes in boundary layer profile with Reynolds number and Rossby number, and the critical Reynolds number for instability as a function of Rossby number.

It appears that the instability labelled Type II by Faller always occurs first, and at zero Rossby number the critical Reynolds number is 56 ± 2. This instability originates in the Ekman layer, but at slightly higher Reynolds number the fluctuations persist far into the geostrophic region, probably as inertial waves excited by the fluctuations in the boundary layer.

At higher Reynolds number another instability appears of shorter wavelength and slower speed. This instability is confined to the boundary layer and is apparently the Type I originally reported by Faller.

The phase speeds, frequencies and wave front orientations of both type instabilities have been measured.

(The principal results of this research were presented by the author at the Symposium on Rotating Fluids sponsored by the International Union of Theoretical and Applied Mechanics, La Jolla, California, March 28 to April 2, 1966.)

ACKNOWLEDGEMENTS

The author would like to express his sincere thanks to Professor Erik L. Mollo-Christensen for his advice and unfailing confidence during the course of these experiments; and to the U. S. Navy for allowing him to pursue a full time course of graduate study while on active duty. The author is also indebted to R. DiMatteo for his help with the electronic equipment and to Mrs. J. McNabb and Miss P. Freeman who typed the manuscript.

This work was made possible by the financial support of the National Aeronautics and Space Administration, Grant NASA NsG-496.

TABLE OF CONTENTS

ILLUSTRATIONS

SYMBOLS

A	Eddy viscosity
C	Phase velocity
C_p	Specific heat at constant pressure
d	Diameter
D	Ekman depth
E	Internal energy
f	Instability frequency in cps; also Coriolis parameter
H	Total fluid depth
I	Amperage
k,l,m	Components of the vector wave number
k	Thermal conductivity
ℓ	A length
n	Nusselt number
p	Pressure
P	A modified pressure $p/\rho + \Omega^2 r^2/2 - gz$
P_r	Prandtl number
Q	Internal heat
r	radius
R	Resistance
Re	Reynolds number
Ro	Rossby number
S	Mass flow rate
S^*	Computed boundary layer transport

T	Temperature
Ta	Taylor number
u,v,w	Perturbation velocity components
U	Velocity
$\bar{V}$	Velocity vector
V_g	Measured geostrophic velocity
V_r	Radial velocity
V	Theoretical tangential velocity
$V(2)$	2nd order tangential velocity
W	Work; also the width of a vertical boundary layer
x,y,z	Rectangular coordinates
z'	Non-dimensional height
δ	Measured boundary layer thickness
δ^*	Boundary layer displacement thickness
ε	Angle between the wave front and the tangential direction, measured in the sense that the Ekman spiral makes a positive angle
θ	Angle between the double wire axis and the tangential direction
λ	Wavelength
μ	Fluid dynamic viscosity
ν	Fluid kinematic viscosity
ρ	Fluid density
σ	Statistical standard deviation
ϕ	Angle between the hot wire and the flow direction
ψ	Latitude

ω	Instability frequency in radians per second
Ω	Tank rotational frequency
$( )_a$	Evaluated at ambient conditions
$( )_c$	Critical value

CHAPTER I

INTRODUCTION

I.1 Review of Previous Work

During the drift of the FRAM across the polar sea (1893-1896), Fridtjof Nansen observed that the direction of drift of the surface ice was 20 degrees to 40 degrees to the right of the wind, and attributed this phenomenon to the effect of the earth's rotation. Nansen further reasoned that the direction of motion of each water layer must be to the right of the layer above it since it is affected by the overlying layer much as the surface layer is affected by the wind. (Sverdrup, Johnson, and Fleming [1])

At Nansen's suggestion, V. W. Ekman [2] undertook the mathematical analysis of this problem, and investigated the flow resulting from a balance of pressure gradient, coriolis, and frictional forces. Ekman considered the eddy viscosity, A, to be constant; and showed that the important boundary layer velocities are confined to a layer of thickness $\sqrt{A/\rho f}$, which Ekman called the "depth of frictional resistance". Within the boundary layer, the velocity is represented by a vector which changes in length exponentially with depth, and in angle linearly with depth. This is the familiar Ekman Spiral. Although Ekman considered an eddy viscosity, the analysis is applicable to laminar flows if the constant eddy viscosity A is replaced by constant dynamic viscosity μ . The Ekman solution for the components of a bottom boundary current under a velocity V in the

x direction which is independent of depth is given by:

$$V_x = V(1 - e^{-Z/D}\cos(Z/D))$$

$$V_y = Ve^{-Z/D}\sin(Z/D)$$

Because of the similarity in the boundary layer profiles in Ekman flow and the flow over a rotating disc in a fluid at rest (Schlichting [3]), it is interesting to consider the results of some early instability experiments with rotating discs in free air. In 1944, Theodorsen and Regier [4] made measurements with a fixed hot wire anemometer over a disc rotating in free air, in which they found a disturbance occurred at a transition Reynolds number of 1440, with the following definitions:

$$Re_\delta = \frac{(\Omega r)\delta}{\nu} \quad ; \quad \delta = 2.58\sqrt{\nu/\Omega}$$

This corresponds to a Reynolds number of 560, when Re is defined as:

$$Re = \frac{(\Omega r)}{(\nu\Omega)^{\frac{1}{2}}}$$

In 1945, Smith [5] used a hot wire probe adjacent to a vertical rotating disc in air, and found sinusoidal disturbances to occur at:

$$620 < Re_{\delta*} < 760$$

where: $\delta* = 1.37\sqrt{\nu/\Omega}$

Eliminating the 1.37 factor, this corresponds to a Reynolds number range of:

$$450 < Re < 555$$

Smith, using a double wire probe, determined the phase velocity to be $C = 0.2(r\Omega)$, and the angle of orientation to be 14 degrees with respect to the tangential direction.

In 1955, Gregory, Stuart, and Walker [6] used the china clay technique to determine the presence of instability on a rotating disc in free air. This technique is limited in that it is capable of demonstrating the presence only of stationary modes of disturbance. They found that an instability occurred at $Re = 1.8 \times 10^5$, with the Reynolds number defined as:

$$Re = \frac{(\Omega r)r}{\nu}$$

This reduces to a critical Reynolds number of 435 when the second r is replaced by the Ekman depth D in the computation of Re.

The direction of propagation of the waves as given by the china clay picture was 14 degrees from the radial direction, in good agreement with Smith's work and the theoretical calculations of Stuart in the same paper. Stuart's mathematical analysis indicated the instability to be in the form of a series of horizontal roll vortices with spacing related to the boundary layer depth; an hypothesis which was reasonably well confirmed by the experimental work. Stuart concluded that the curvature terms had little influence on this inviscid instability.

In 1960, Stern [7] considered the theoretical problem of a fluid of relatively shallow depth in a rotating annulus, with fluid being forced in at the outer rim and withdrawn at the inner rim. This establishes a geostrophic azimuthal velocity over an inflowing viscous boundary layer. Stern theoretically established the possibility of the existence, at large Taylor numbers, of an instability which draws its energy from the ageostrophic perturbation component of the mean flow. He referred to this as a "body-boundary" mode, and suggested that for Taylor numbers as large as 2.5×10^3 the flow should be unstable at Reynolds numbers below 80; and that the preferred mode of disturbance should have a radial wavelength given by:

$$\lambda_r = \frac{2\pi}{m} Ta^{\frac{1}{4}} D$$

where Ta is the Taylor number:

$$Ta = \frac{\Omega H}{2}^2$$

H is the total fluid depth, and m is a constant of order unity.

In 1961, Arons, Ingersol, and Green [8] conducted a series of experiments in which they supplied water to the center of a rotating tank partially filled with water, and allowed the surface to rise with time. They observed a highly organized pattern of instability in the form of concentric cylindrical sheets of water which rose as sharply defined jets through the entire depth of the fluid. This instability was confined to the narrow Reynolds number range:

$$1.6 < Re = \frac{VD}{\nu} < 3.6$$

and had a wavelength given by

$$\lambda = 2.0\ Ta^{\frac{1}{4}} D$$

Faller conducted both a theoretical and an experimental study of Ekman layer instability in which he considered a rotating tank partially filled with fluid having a distributed source around the outer rim and a concentric sink at the center. His theoretical analysis [9] utilized an expansion in Rossby number of the non-dimensionalized dependent variables of the Navier-Stokes equations (see Fultz [10]) to form an ordered set of equations which could be solved subject to the appropriate boundary conditions. He found the radial component of the interior flow to be zero to the second order, and the non-dimensional second order tangential velocity to be given by:

$$V(2) = 1 - \frac{3}{10} R_o + \frac{233}{300} R_o^2$$

For his experimental work, Faller [11] used a rotating tank 4 meters in diameter with a pumping system to withdraw water from the center and distribute it uniformly around the outside. The boundary layer circulation was observed by the introduction of potassium permanganate dye crystals near the outer rim, which tended to form streaklines as the fluid flowed past. Spiral bands of dye which formed were interpreted as regions where the layer of dyed

fluid became deeper or shallower due to the superposition of unstable perturbations on the basic boundary layer flow. Photographs of the bands were measured to give a critical radius at which the bands were first observed, their orientation, and their spacing.

Faller used the zero-order solution for the geostrophic velocity:

$$V_\theta = \frac{S}{\pi r D}$$

where S = mass flow rate in the definitions of Reynolds number and Rossby number:

$$Re = \frac{S}{\pi r \nu} \quad ; \quad Ro = \frac{S}{2\pi r^2 \Omega D}$$

so that both parameters could be expressed in terms of only the two independent parameters, S and Ω. The critical Reynolds number, in the limit of zero Rossby number, was found to be 125 ± 5. The wavelength, non-dimensionalized by the Ekman depth, varied from 9.6 to 12.7 with an average of 10.9. The average angle from the tangential direction was found to be $\varepsilon = 14.5$ degrees to the left, with a standard deviation of 2.0 degrees. Motion pictures of the bands showed that in all cases they moved radially inward.

Barcilon [12], in a 1965 theoretical paper, obtained analytic solutions of the perturbation equations using an Ekman mean velocity profile. He did not, however, arrive at a value for a critical Reynolds number since his method of solution was not accurate at the relatively small Reynolds numbers where instability has been observed.

He concluded that at large Reynolds numbers, the Coriolis force does not affect the stability properties of the Ekman layer; and that in this respect the Coriolis force does not play a significant role in the stability analysis. This is essentially in agreement with the deductions of Stuart (GSW) who analyzed the inviscid equations for flow over a rotating disc.

Lilly [13] and Faller and Kaylor [14] at about the same time presented numerical solutions to the Ekman layer problem. Lilly used a perturbation analysis and numerically solved both the complete set of equations and the Orr-Sommerfeld equation (OSE). Both solutions exhibited instability, with a minimum Reynolds number of 55 for the complete set and 85 for the OSE. Stationary waves were found to be unstable above Re = 115. Lilly suggested that the substantially lower critical Reynolds number for the complete set indicated the existence of a separate instability mechanism, associated with the Coriolis terms; and verified this by means of a simplified analytic solution. He designated this as a "parallel instability", and noted that it was of the viscous type since it vanished at high Reynolds numbers. The numerical solution indicated that the viscous instability should be oriented at small or negative (to the right) angles with respect to the tangential flow.

Faller and Kaylor obtained numerical solutions to the time dependent non-linear equations of motion starting with a perturbation on the finite difference equivalent of a laminar Ekman solution. Their results confirmed the presence of two distinct modes

of instability; one with $\lambda = 11D$ and $\varepsilon = 12$ degrees, and a longer faster wave at negative ε with a critical Reynolds number in the range $50 < Re < 70$.

In a recent experimental paper, Faller and Kaylor [15] have reported the observation of the viscous instability occurring at lower Reynolds number, which they have designated Type II. The apparatus used was essentially the same as was used earlier by Faller (1963) in his studies of the inviscid instability waves (Type I). The Type II waves were found to occur sporadically, move rapidly, have a wave length of 22 to 33 times the Ekman depth, and to be oriented at an angle varying from 5 degrees to the left (+5 degrees) to 20 degrees to the right (-20 degrees) of the tangential direction. These waves occurred at a minimum Reynolds number $Re = 70$. It was observed that when the Type II vortices attain finite amplitude before the Type I are established, the combined circulation becomes unstable to a small scale mode, which then interacts with the previously established flow to produce an abrupt transition to turbulence.

At the time the present investigation was initiated, Faller's 1963 paper was the most recent experimental investigation available, and it was felt that his observational techniques using dye and photography were sensitive only to stationary or at best slowly moving waves. In none of the works cited have quantitative measurements been made in either the mean flow or the boundary layer for the Ekman model. Our experiment was designed, and the equipment

built, to allow the quantitative measurement of Ekman boundary layer parameters.

I.2 Description of Experiment

Ekman boundary layers were generated by the removal of air from the center of a rotating tank having the general shape of a large flat spool. Room air was admitted from the outside after passing through a pair of screens to bring it up to solid body rotational speed. The apparatus was specifically designed to utilize air as the working fluid to allow the use of hot wire anemometers in making quantitative measurements.

Measurements were made of the vertical and radial velocity profiles, the boundary layer depth, and the onset of instability using a single wire probe. Wave front orientation and phase velocity were determined using double wire probes.

The instrumentation was designed so that most of the data was available in the form of voltages, allowing the use of an X-Y recorder and a high speed pen recorder to monitor continuous profiles as parameters were changed.

CHAPTER II

EXPERIMENTAL EQUIPMENT

II.1 The Rotating Tank

Figure 2.1 is a schematic diagram and figure 2.2 is a photograph of the rotating tank which was built for this experiment. The main body of the tank consists of two 36 inch diameter plates of one-half inch plexiglass; held 3.00 inches apart by a hollow core at the center and six spacers around the outer rim. It is supported by a hollow shaft running in two main bearings; and driven in rotation by a V-belt from an auxiliary shaft, which receives its power from an electric motor and variable speed hydraulic unit. The hollow shaft is connected through a flowmeter to the suction side of a potentiometer-controlled vacuum cleaner. Around the outer rim a 50 mesh silk screen was installed, with another similar screen held one-half inch further out by means of spacers. These screens served to bring the incoming air up to solid rotation speed before it entered the tank. A plexiglass baffle between the outer edges of the upper and lower plates restricted the space through which air could enter to the 0.62 cm space adjacent to the plates. Another silk screen was placed at a three inch radius around the central hub. The entire system was supported by a frame of steel beams, and levelled by means of adjustments at the four corners.

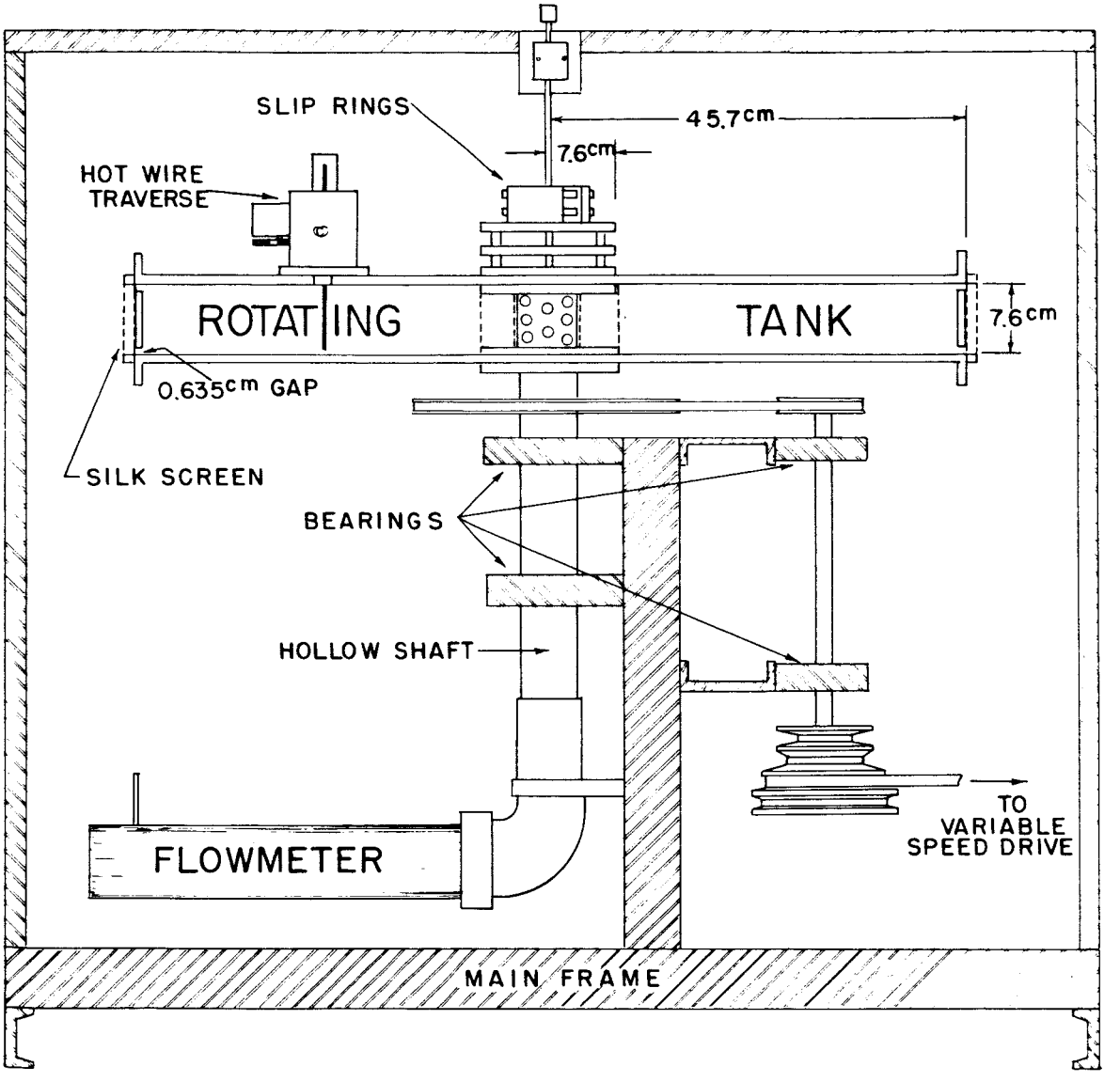

Figure 2.1 Schematic diagram of rotating tank

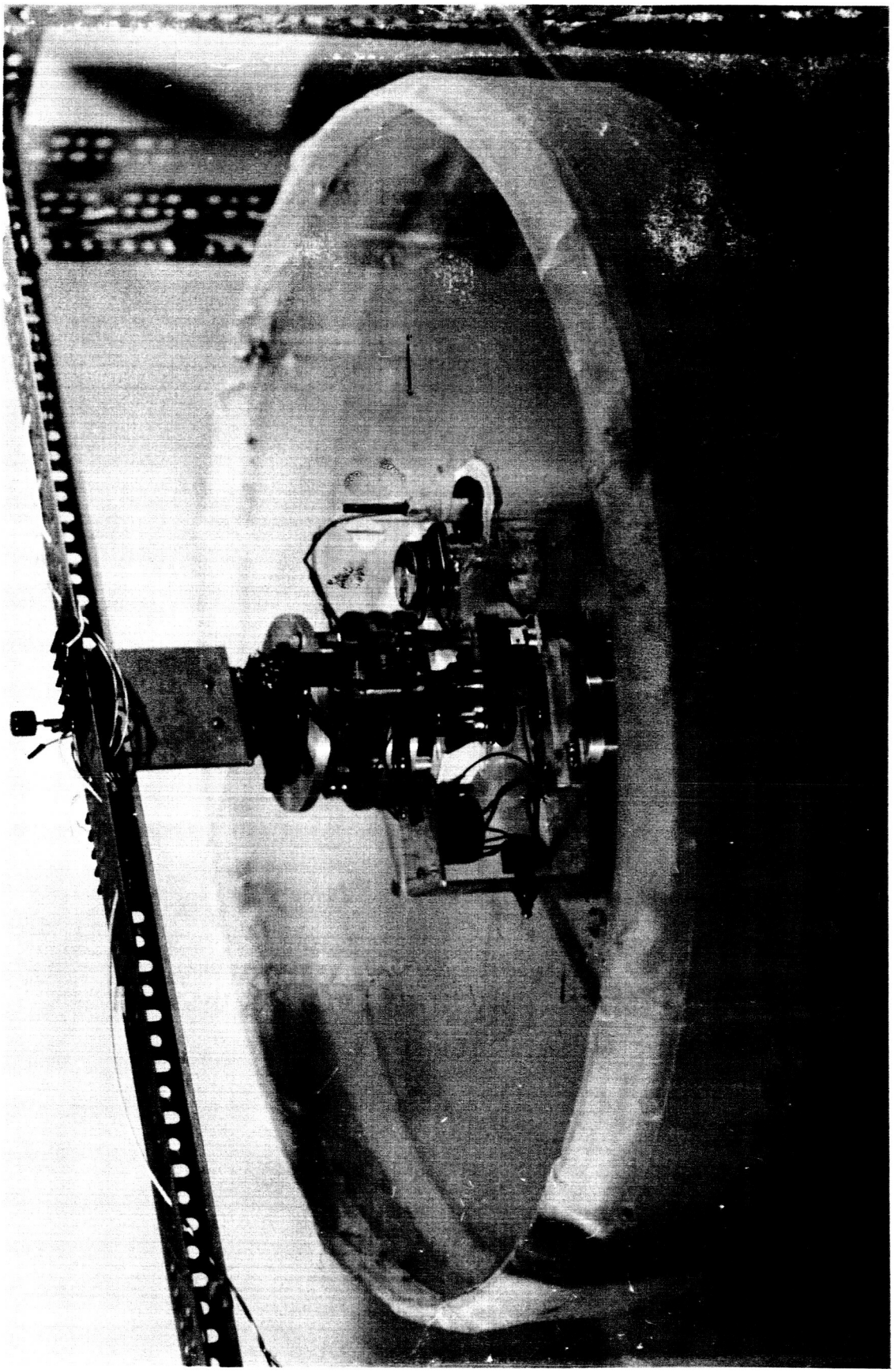

Figure 2.2 Photograph of rotating tank

Five three-fourth inch holes were drilled in the upper plate of the tank, at radii of 6, 8, 10, 12 and 14 inches, to allow the insertion of hot wire probe assemblies.

On the top of the tank a slip ring assembly was installed, consisting of nine silver rings each with two silver graphite brushes. A lightweight frame extended over the top of the tank to hold the fixed portion of the slip ring assembly.

II.2 The Flowmeter

The flowmeter, figure 2.3, consisted of a brass pipe 18 inches long and 2 inches in diameter, with silk screens across the upstream end to smooth the flow, a one-eighth inch rod across the flow 12 inches downstream, and a hot wire probe 1 inch further downstream. The Strouhal shedding frequency (Roshko [16]) of the cylinder across the flow was sensed by the hot wire anemometer, amplified, and counted by the electronic frequency counter. In this case, no calibration of the hot wire is necessary, and the hot wire circuit can be reduced to its fundamentals. The hot wire is placed in series with a dry cell battery and a large resistance; the voltage fluctuations across the hot wire measure the shedding frequency. This frequency was calibrated in terms of mass flow by placing a small wind tunnel downstream in series with the flowmeter, while the flowmeter was mounted on the tank. Four silk screens at intervals of 1.5 inches smoothed the flow before it entered the test section. The velocity profile in the test section was determined with a previously calibrated

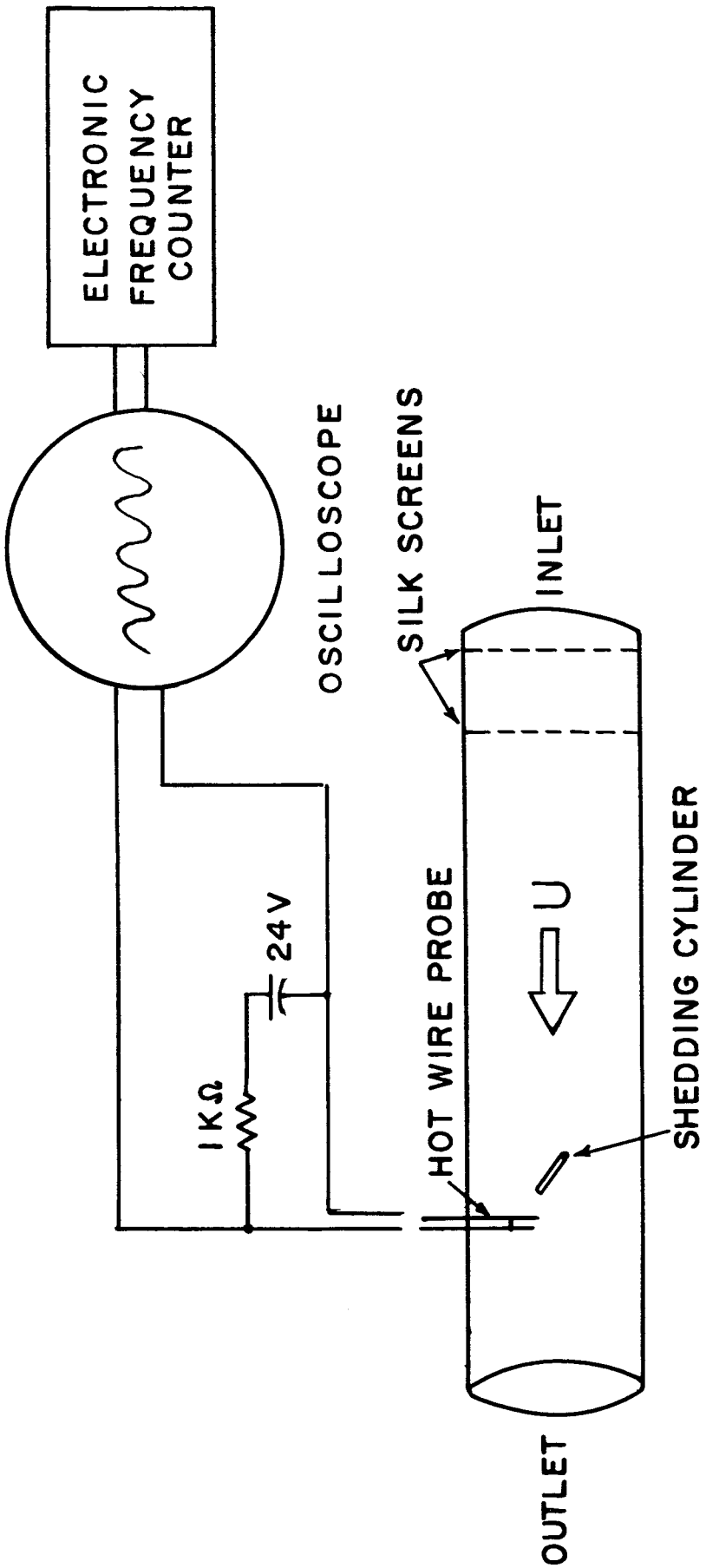

Figure 2.3 Schematic diagram of flowmeter

hot wire anemometer, the displacement thickness δ^* computed as a function of velocity (Rosenhead [17]), and from this the net mass transport computed as a function of velocity. The results of this calibration procedure are shown in figure 2.4.

II.3 The Traversing Mechanism

A traversing mechanism was constructed which mounted on the upper plate of the tank and allowed a probe to be driven vertically or angularly while the tank was rotating (figure 2.5). A micrometer barrel was incorporated into the vertical positioning drive which allowed precise control and calibration of vertical position. A ten-turn precision potentiometer was geared to the micrometer barrel allowing the calibration of vertical position in terms of a direct current voltage taken out through the slip rings. Similarly, the stem of the probe was geared to a continuous turn precision potentiometer which allowed the angular position of the sensing wire to be calibrated in terms of a voltage. Mercury cells rotating with the traversing mechanism were used in conjunction with the potentiometers to conserve slip rings. A 24 volt potentiometer controlled d.c. motor could be used to drive the probe either vertically or angularly, and a double pole double throw switch connected the appropriate potentiometer to the battery supply and the output slip rings.

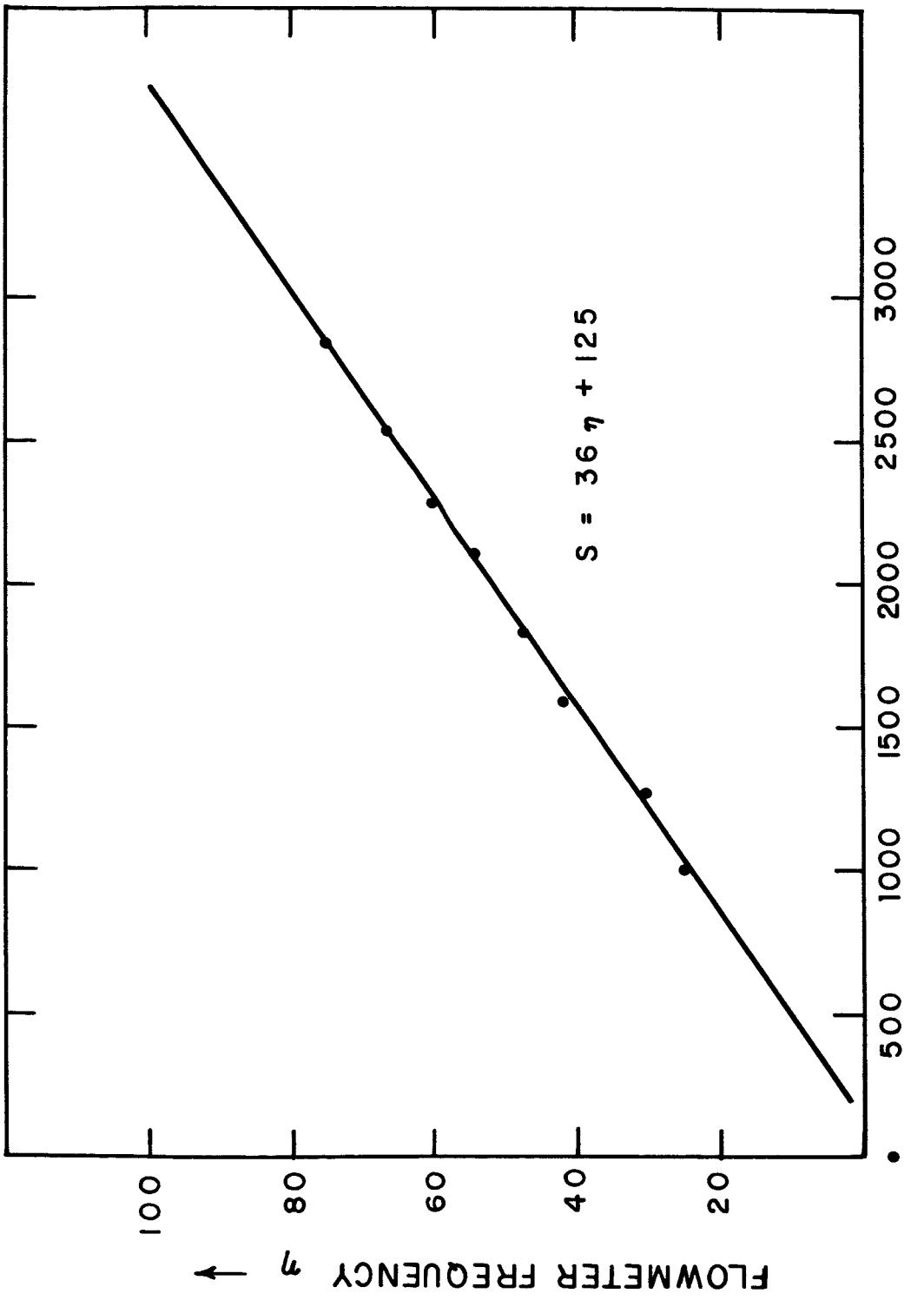

Figure 2.4 Flowmeter calibration curve

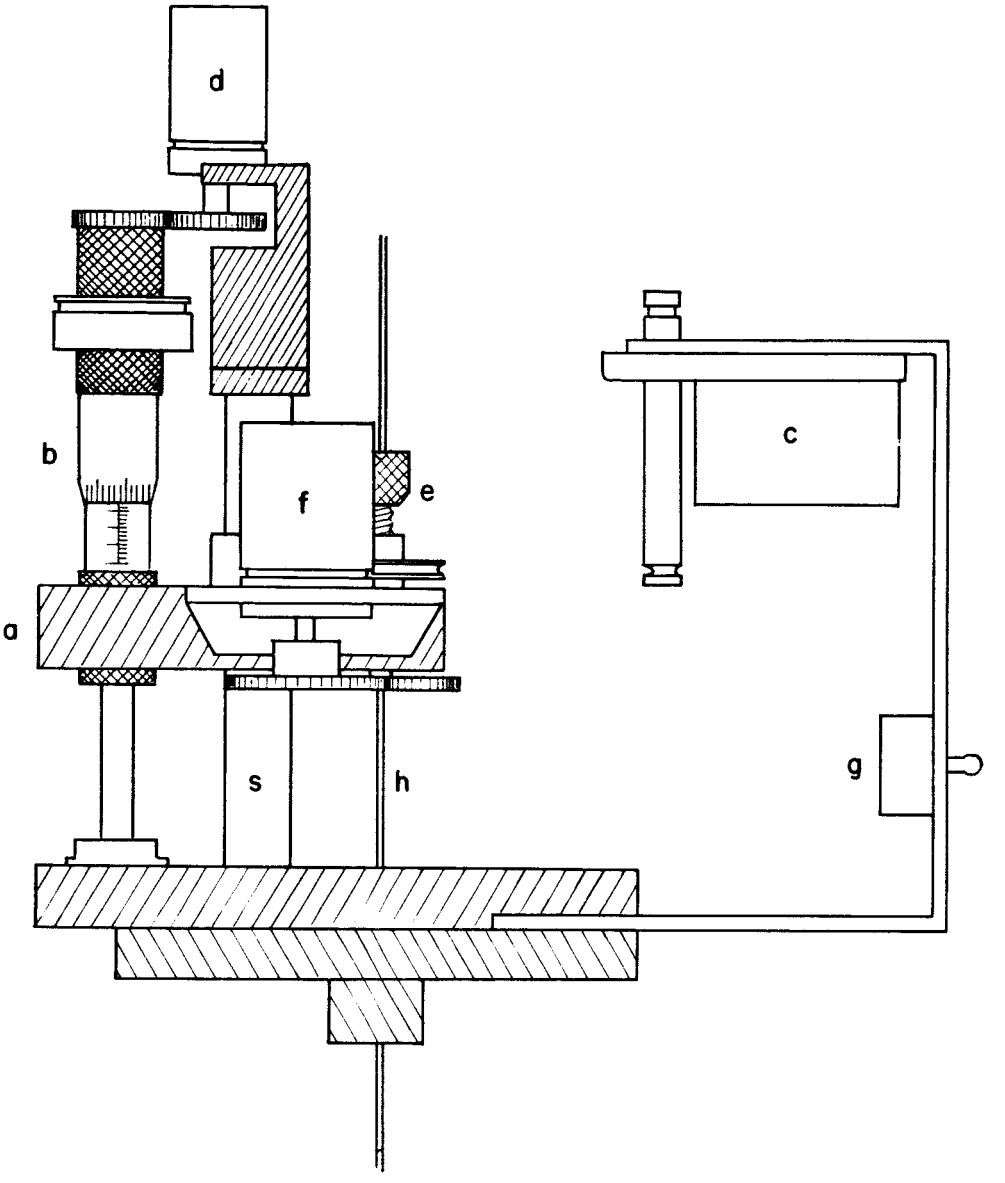

The moveable block a is driven vertically on shaft s by the micrometer head b, which may be connected by belt to the externally controlled motor c. A ten-turn precision potentiometer d is geared to the micrometer. Alternately, the motor may be connected by belt to drive the holder e containing the hot wire h. A continuous turn potentiometer f is geared to the hot wire.

Figure 2.5 Schematic diagram of traversing mechanism

II.4 The Hot Wires

Three basic hot wire probe designs were used; all utilized 0.00016 inch diameter platinum 10 per cent Rhodium wire as the sensing elements. The fundamental probe, which was used for the detection of the instability and all qualitative measurements (figure 2.6), consisted of a 0.10 inch stainless steel tube as the probe stem, and two ordinary sewing needles attached to the end with a 0.16 inch point spacing as the hot wire supports. This probe was designed to fit into and used exclusively with the traversing mechanism. A variation of this single wire probe was the bent probe. This was made by bending the stem of the basic probe to a right angle 2.91 inches from the sensing wire. The bend was made such that the wire was parallel to the original stem. When this wire was inserted into the traversing mechanism, the sensing wire swept through circle as the stem was rotated.

A second probe used was one which had two parallel horizontal hot wires 0.125 inch long spaced 1.6 mm apart (figure 2.7). This was designed such that the underside of the probe mount was flush with the inside of the top plate of the tank when the probe was installed. The needles supporting the hot wires extended 3 mm into the tank, and the entire probe was fixed to a large gear. This probe was driven in rotation at a fixed rate of 3^{o} sec^{-1} by an externally controlled a.c. synchronous motor.

The third probe (figure 2.8) was similar to the second except that the sensing portions of the wires were vertical, 0.10 inch long, and 6 mm from the upper boundary.

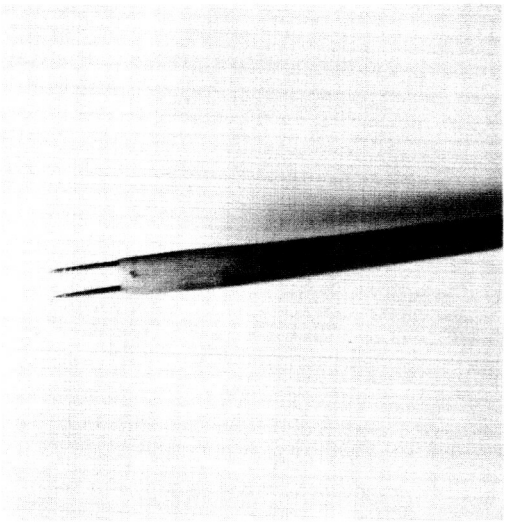

Figure 2.6 Photograph of single wire probe

Figure 2.7 Photograph of double wire probe with horizontal wires

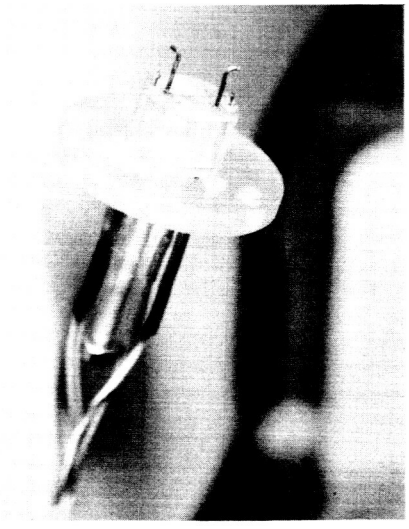

Figure 2.8 Photograph of double wire probe with vertical wires

II.5 Associated Electronic Equipment

The associated electronic equipment used in these experiments is briefly described here and shown in figure 2.9.

Hot Wire Equipment. All hot wire measurements, excluding the flowmeter, utilized the constant current hot wire system manufactured commercially by Transmetrics, Inc. This system is composed of a current control panel for supplying and controlling the current to two hot wires, a bridge for measuring wire resistance, and a potentiometer for measuring voltage and current.

Oscillator. A Hewlett-Packard Model 202C low frequency oscillator was used for Lissajous figures in hot wire calibration, and as a signal generator for calibration purposes when operating with two wires.

X-Y Recorder. A Plotomatic Model 600 X-Y recorder was used to convert d.c. voltages to x,y coordinates.

Electronic Counter. A Hewlett-Packard Model 522B electronic counter was used in conjunction with the flowmeter.

Oscilloscope. A Tektronic Model 502 dual beam oscilloscope was used for displaying instantaneous voltages across the hot wires, and for Lissajous figures.

Amplifiers. Two Keithly Model 102B decade isolation amplifiers were used to boost the hot wire signal when necessary.

Recorder. A Sanborn Model 67-1200 pen recorder was used for phase comparison of two signals.

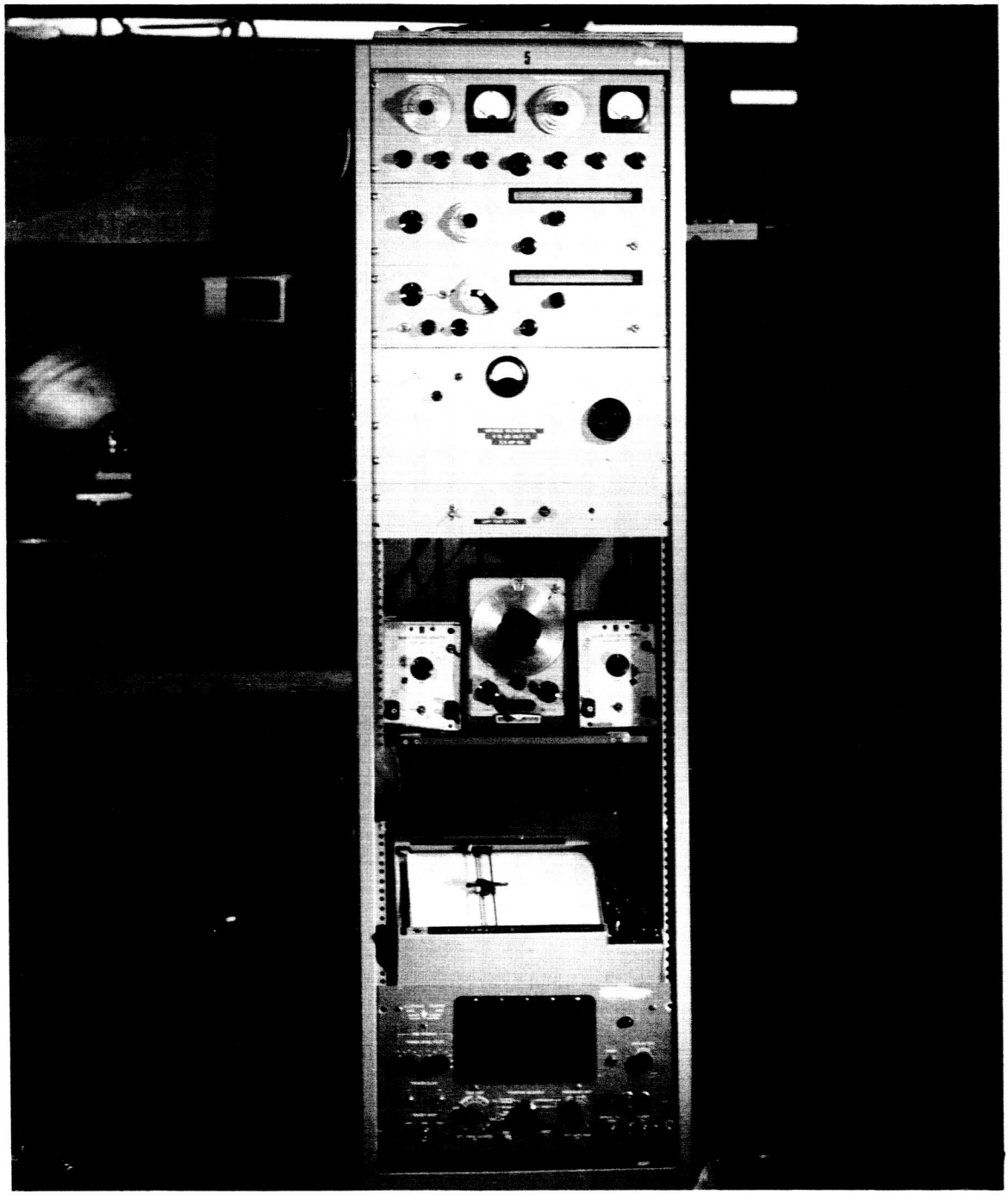

Figure 2.9 Associated electronic equipment

CHAPTER III

EXPERIMENTAL TECHNIQUES

III.1 Measurement of a Velocity Vector

Since a hot wire anemometer is primarily sensitive to the component of flow at right angles to the wire, it can be used to determine direction as well as magnitude of velocity. The wire indicates a maximum velocity when it is perpendicular to the flow, and a minimum when parallel. The velocity indicated by a hot wire is closely approximated by:

$$U_{indicated} = U_{max} \sin \phi$$

where ϕ is the angle between the wire and the flow direction.

For the determination of a velocity vector, the hot wire was first calibrated in a wind tunnel (see A.4). The hot wire output signal was then biased to remove a portion of the d.c. signal, and the remaining signal was used to drive the X-axis of the X-Y recorder. The Y-axis of the recorder was driven by the d.c. voltage output of the continuous turn potentiometer on the traversing mechanism. The motor of the traversing mechanism was connected by belt to drive the probe angularly. With the tank rotating, suction applied, and steady-state conditions established within; the probe was slowly rotated through 360^{o} with the X-Y recorder plotting velocity versus angular position (figure 3.1)

When it was particularly desireable to have maximum accuracy

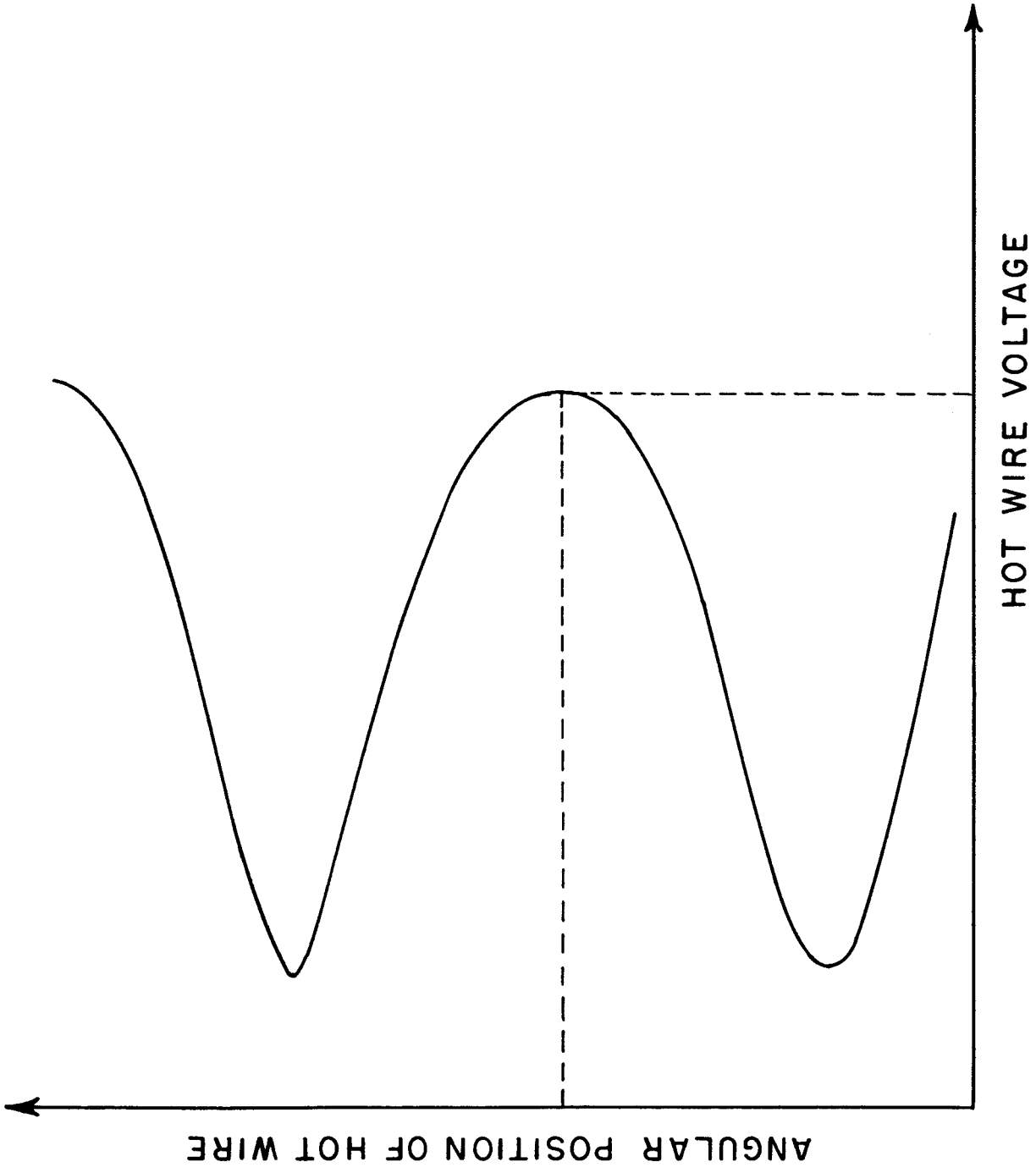

Figure 3.1 Typical velocity versus hot wire angle curve for the determination of the velocity vector

in the determination of $|V_g|$, and periodically to check the calibration of the hot wire, a different technique was used. In this method, the probe was set to be perpendicular to the flow with the tank operating, and the hot wire set potentiometer balanced. The tank was then stopped, and the entire traversing mechanism containing the probe, still connected through the same wiring and slip rings, was placed in the test section of the calibration wind tunnel which was adjacent to the tank. The tunnel velocity was adjusted until the potentiometer was again balanced. A cylinder of known diameter was then inserted across the test section upstream from the hot wire, and the Strouhal shedding frequency determined by the use of an oscillator and an oscilloscope to draw Lissajous figures (see A.4). The indicated oscillator frequency was checked with an electronic frequency counter. The velocity determined by this method is considered to be accurate to within $\pm$ 0.5 cm sec^{-1}.

III.2 Profiling the Boundary Layer

To get an accurate calibration of the vertical position of the hot wire, the probe was lowered very slowly until the wire supporting needles just touched the bottom boundary. At this point the reading of the micrometer barrel, graduated in thousandths of an inch and easily readable to 0.0005 inch, was recorded. Then as the probe was moved up, the readings of the micrometer could be directly converted to height off the bottom, z. To obtain vertical profiles of the horizontal velocity; the probe was set 0.010 inch off the bottom

the tank started at a fixed rotation rate, and the suction started. For the remainder of the operations, the suction rate S and the rotation rate Ω were held constant. When steady state had been achieved, the velocity vector was obtained as III.1. The tank was then stopped, the probe was raised 0.025 inch, and the procedure repeated. This was continued until the probe was 0.04 inch off the bottom. At this height, the velocity vector was showing no change with height; its direction was taken to be that of the geostrophic flow, 0^{o}, and this angle used to calibrate all previous measurements in the series. This method of calibrating angular position, while not ideal, was considered more accurate than any of the other techniques attempted.

III.3 Geostrophic Velocity as a Function of Radius and Height

To plot profiles of geostrophic velocity versus height, it was necessary to calibrate the Y-axis of the X-Y recorder against the potentiometer geared to the micrometer barrel, after calibrating the micrometer as in III.2. The direction of the geostrophic flow was determined as previously, and the hot wire was set perpendicular to that direction. The motor on the traversing mechanism was then connected by belt to the micrometer drive, and the tank rotation and suction started. Starting from z = 0.002 inch (the vertical traverses were always started from the lowest point to preclude inadvertent contact of the wire with the bottom since this generally resulted in a broken wire), the probe was driven vertically at a rate of

approximately 0.005 in sec^{-1} up to z = 0.40 inch. This rate of vertical drive was sufficiently slow as to have no noticeable effect on the output; reversing the direction of motion and profiling back down through an area already covered yielded the same results.

On those runs where it was desired to continue the profile above z = 0.40 inch, it was necessary to reposition the probe in the traversing mechanism. While this repositioning was not possible with the same accuracy as the initial vertical calibration, it was accurate to within $\pm$ 0.010 inch.

Determining the velocity as a function of radius was considerably more difficult. Since the tank design permitted measurements only at five fixed stations, the slow smooth radial traverse which was desireable was not possible. The means of measuring $V_g(r)$ was found to be a bent probe. In rotating this through 360° the sensing element swept through a circle of 5.82 inch diameter; thus measurements taken at two adjacent measuring stations separated by 2 inches in radius overlapped each other. To obtain $V_g(r)$ it was necessary to make a 360° sweep with the X-Y recorder plotting velocity versus angle at each of the five stations for a fixed S and Ω. A typical plot from such a sweep is shown in figure 3.2. The wake from the probe stem when the sensing element was downstream shows quite clearly in these plots.

III.4 Detection of the Onset of Instability

For this phase of the investigation, a straight single wire

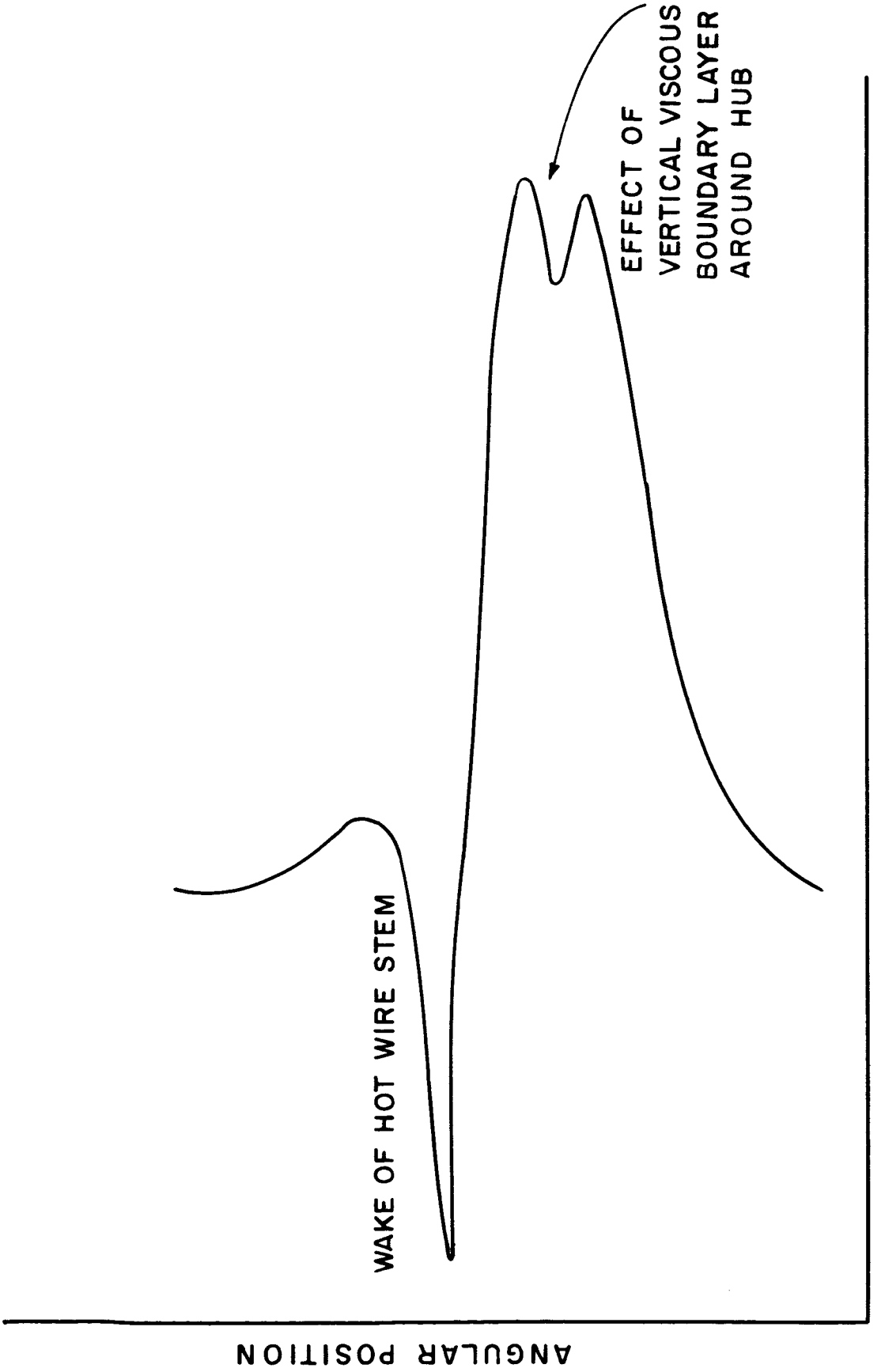

Figure 3.2 Typical plot of hot wire voltage versus radial position showing the inner viscous boundary layer

probe mounted in the traversing mechanism was used. Since fluctuations and not absolute values were being sought; it was not necessary to calibrate the hot wire. Preliminary investigations indicated that the maximum amplitude of the instability signal would be obtained with the hot wire oriented approximately parallel to the geostrophic flow and one Ekman depth off the bottom, so this positioning was used for the systematic investigation of onset of instability.

The hot wire signal, biased to remove most of the d.c. was used to drive the Y-axis of the recorder. The X-axis was operated in the time-sweep mode at one in sec^{-1}. Operating the tank at a constant Ω, the suction S was incrementally increased; the tank allowed to stabilize, and the plotter actuated for one sweep. For relatively low values of S, these sweeps were essentially straight lines. At some point in this incremental increase, however, the hot wire output voltage would begin to oscillate, and these oscillations plotted against time would be sinusoidal in appearance, as in figure 3.3. When this occurred S would by systematically varied downward in smaller increments until the lowest setting at which instability occurred was determined. No hysteresis was noticed between the critical points obtained by increasing or decreasing Reynolds number. At the critical point, the flowmeter frequency n, the rotation rate Ω, and the radius of the probe r were recorded.

III.5 Determination of the Boundary Layer Thickness

For the determination of boundary layer thickness, the equipment

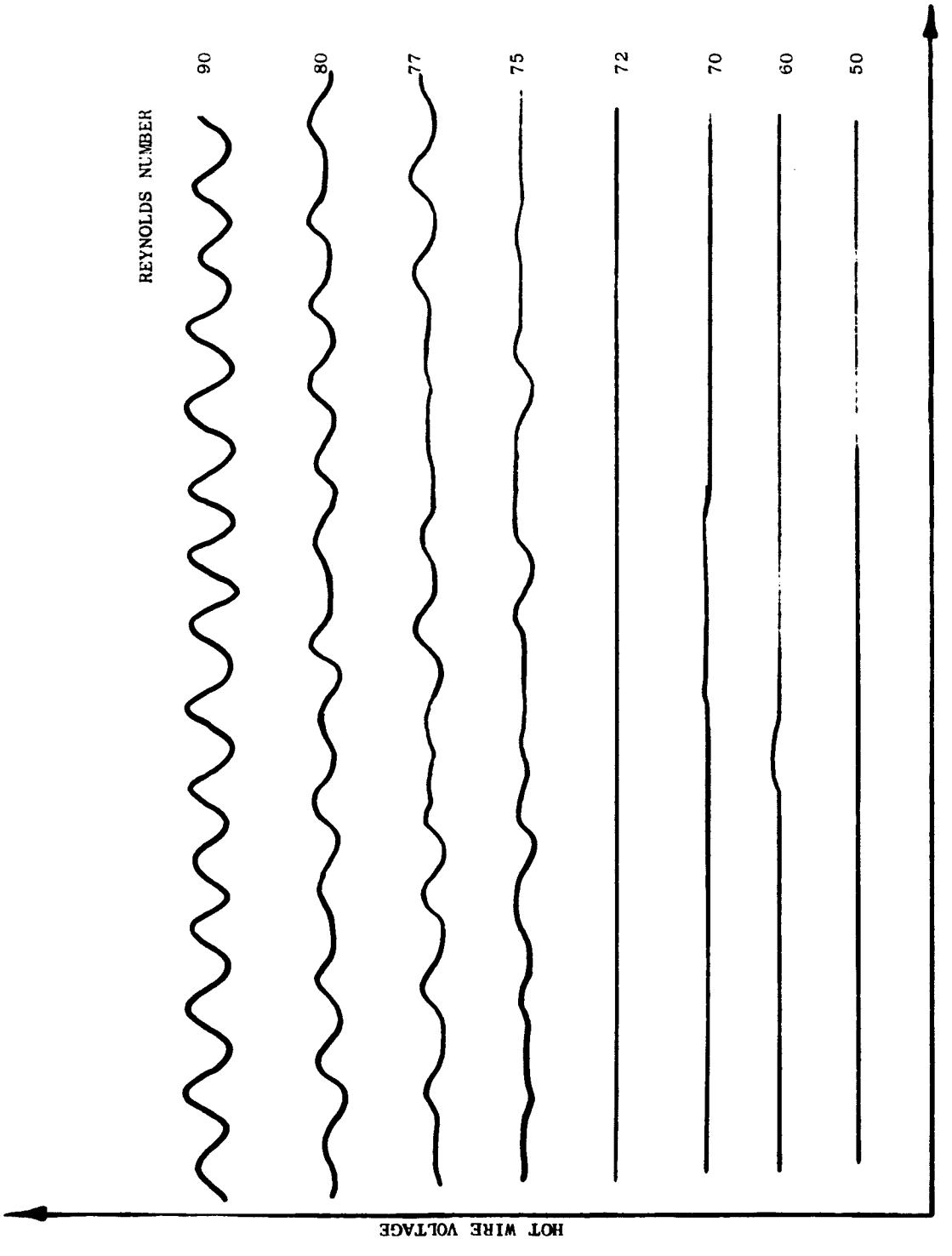

Figure 3.3 Plot of the hot wire voltage versus time as a function of mass flow for the detection of the Type II instability

was set up as in the case of vertical profiling of geostrophic velocity (section III.3) except that in this case the probe was set parallel to the direction of the geostrophic flow ($\phi = 0^o$). As the probe was driven vertically upward, the recorder plotted a profile of radial velocity V_r versus height. These profiles, as shown in figure 3.4 exhibited the characteristic shape of theoretical V_r profiles. The apparent sharp increase in velocity at the bottom is an artifact caused by loss of heat from the wire to the boundary (Wills, [18]). The theoretical Ekman radial velocity reaches a maximum at $z/D = \pi/4$; the measured boundary layer thickness δ was computed by measuring the z coordinate of the maximum in the V_r profile, and taking $\delta = 4z/\pi$.

III.6 The Change of the Instability

The hot wire signal, as monitored on an oscilloscope or recorder, is quite regular in appearance with increasing Reynolds number from the critical point Re_c up to a second well defined point. At this point, the character of the wave changes markedly and quickly. Figure 3.5(a) shows the appearance of the wave at a Reynolds number just below this point, and figure 3.5(b) shows its appearance at this point. There is a 3% difference in Re between the two charts. It appears that a second or different instability mechanism has taken place. When this change occurred, the pertinent parameters were recorded. It was noted, however, that this marked change was observed only when the hot wire was close to the boundary. The change of wave character as

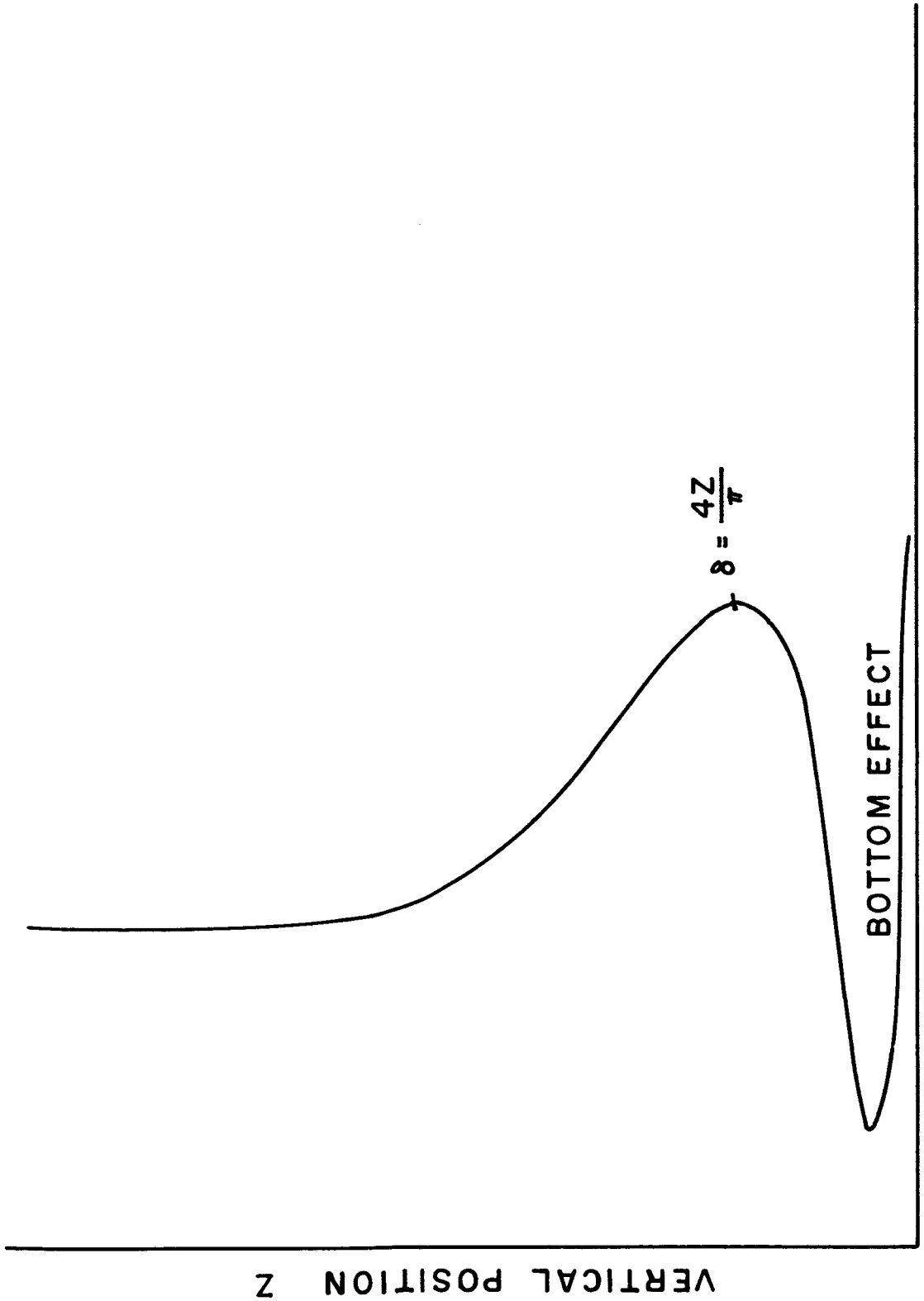

Figure 3.4 Vertical profile of the radial velocity component for the determination of the boundary layer thickness

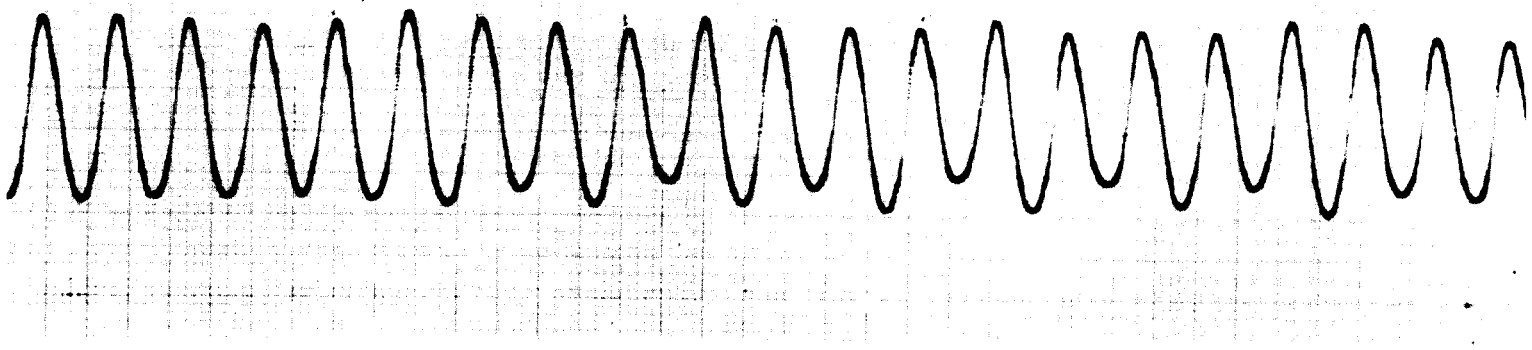

WAVE FORM AT REYNOLDS NUMBER = 126

WAVE FORM AT REYNOLDS NUMBER = 130

Figure 3.5 Hot wire output as a function of Reynolds number showing the onset of the Type I instability

shown in figure 3.5 was detected with the double horizontal probe, which had its sensing wires 3 mm from the boundary. This change was not observed when using the double probe with vertical wires, which measured at 6 mm from the boundary.

III.7 Measurement of Wave Parameters

By utilizing one of the probes having two sensing wires, it was possible to make phase comparisons of the signals. The signal from one wire was used to drive the horizontal axis of the oscilloscope, and the signal from the other the vertical axis. In addition, both signals were fed through the Keithly amplifiers and used to drive two channels of the Sanborn recorder. When the signals from the two wires were in phase, a line oriented at approximately 45° was displayed on the oscilloscope. The angle of the line is a function of the relative amplitude of the two signals; however, the figure displayed collapses from an ellipse to a line only when the two signals are in phase. In utilizing the recorder to display phase differences, it was necessary to calibrate the system for every slight change of frequency; for while the Keithly amplifiers are excellent in not introducing any phase shift at frequencies above 10 cps, they introduced considerable phase shift in the operating range of 1 to 3 cps. In practice, the low frequency oscillator was used as a signal generator to provide an identical input to both of the amplifiers of the frequency to be measured, and the recorder was run at its highest speed of 100 mm sec^{-1}. This provided an accurate calibration of the

amplifier-recorder system on which to base phase measurements.

To calibrate the angle θ between the tangential direction and a line connecting the centers of the sensing wires, a tangential line was scribed on the tank top passing through the center of the 3/4 inch hole in which the probe was to be mounted. An angular scale made from polar graph paper was then affixed to the top around the hole and aligned with these marks. The top of the probe itself was marked to indicate the direction of the line connecting the sensors. With the probe in place, the angle θ could be read directly from the scale on the tank top. While this method necessitated stopping the tank to read the angle θ, and it would have been more desireable to have a continuous output of angular position, the slight inconvenience did not seem to warrant the expenditure of time necessary to build a more sophisticated device.

In making measurements of the first instability, the double probe having vertical wires was used. It was found that the two signals were in phase at only one orientation of the wires with respect to the tangential direction, and this was taken as the wave front orientation. This angle was well defined, since the Lissajous figure on the oscilloscope went from an ellipse turning in one direction, through a line, to an ellipse turning in the other direction in 5^{o} or less or rotation of the probe.

The phase velocity C of these waves was determined by rotating the probe until the Lissajous figure was close to a circle, and measuring with the Sanborn recorder the time delay between the wave crest

reaching the first wire and reaching the second. With the distance, the time, and the frequency known; the phase velocity C and the wave length λ could be computed.

Although it was desireable to use the probe having vertical wires (since they exhibit no directional preference in the horizontal velocity field) for the measurements of the instability at higher Re, it was not possible (see III.6), and the double probe having horizontal wires was used.

Since a horizontal wire is always sensitive to vertical velocity perturbations, and selectively sensitive to horizontal velocity perturbations; the interpretation of the phase comparisons in this case was more difficult. Although the Lissajous figures were hazy and ill defined most of the time; there were fortunately two orientations at which they seemed meaningful. At only one orientation was the passage through a wave front clearly defined; this was taken as the wave front orientation. With the probe perpendicular to the previously determined angle, the maximum phase difference between the two signals was observed. This was measured on the Sanborn recorder and used to determine wave length. Phase velocity was computed from f and λ.

CHAPTER IV

RESULTS

IV.1 Type II Critical Reynolds Number Based on Mass Flow

Since in theory the tangential component of flow accomplishes no net transport across the tank, the entire mass transport must be accounted for by the radial component. Integrating the basic Ekman form of V_r vertically from Z = 0 to Z = 1.5 inches over a circle of circumference $2\pi r$ yields the transport for the boundary layer on one of the plates. Assuming the same form for the upper and lower boundary layers, and replacing the upper limit of integration by ∞ as is commonly accepted in boundary layer theory:

$$2(2\pi r)\, D \int_0^{\infty} V_\theta\, e^{-Z/D}\, \sin(Z/D)\, d(Z/D) = S$$

which may be integrated directly to give:

$$V_\theta = \frac{S}{2\pi r D}$$

Using this value of V_θ in the definition of Reynolds number:

$$Re = \frac{S}{2\pi r \nu}$$

Similarly, the Rossby number may be defined:

$$R_o = \frac{S}{4\pi r^2 \Omega D} = Re \cdot D/2r$$

The onset of instability as a function of S and Ω was determined

for eighteen cases, six each at three different values of radius. For each of these the theoretical tangential velocity, Reynolds number, and Rossby number were computed. The results, as shown in Figure 4.1, plotted as a family of lines. The data for each radius plotted as a reasonably straight line, with a different line for each radial measuring position.

IV.2 Type II Critical Reynolds Number Based on Geostrophic Velocity

Since there was no obvious reason for assuming the critical Reynolds number to be a function of radius, it was decided to refine Re by measuring the actual geostrophic velocity, V_g. (Hereafter measured values will be referred to as geostrophic, and theoretical velocities as tangential). V_g was measured for each of the eighteen sets of parameters, and a new Reynolds number and Rossby number defined as:

$$Re = V_g D/\nu \quad ; \quad Ro = V_g/2\Omega r$$

were computed. A plot of these results is shown in figure 4.2.

The resulting family of lines is nearly identical in appearance with the previous plot. The lines for each measuring station have the same slope, but are lower by a factor of about ten in Reynolds number. The geostrophic velocity was lower in every case than the tangential velocity.

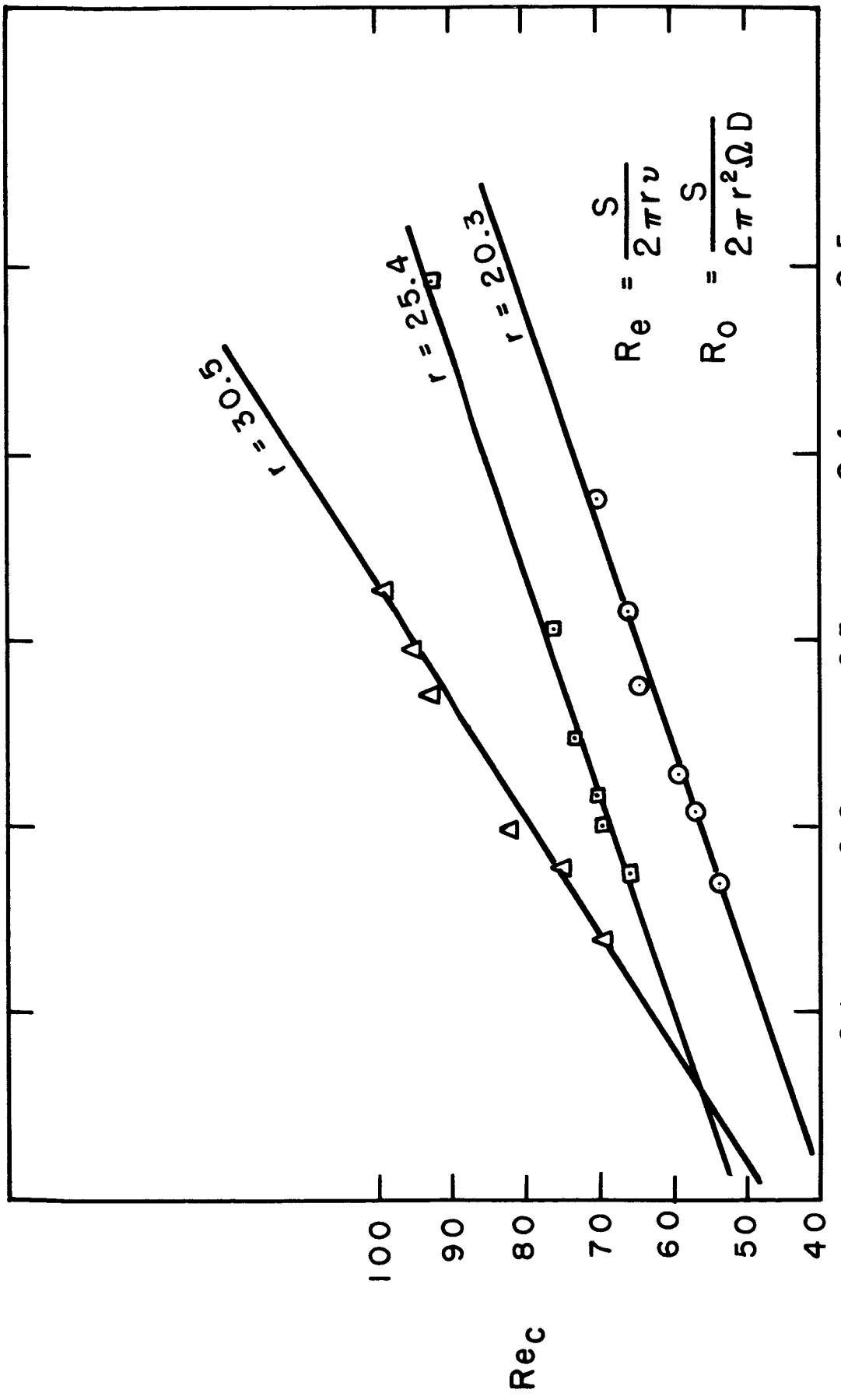

Figure 4.1 Critical Reynolds number versus Rossby number based on the mass flow

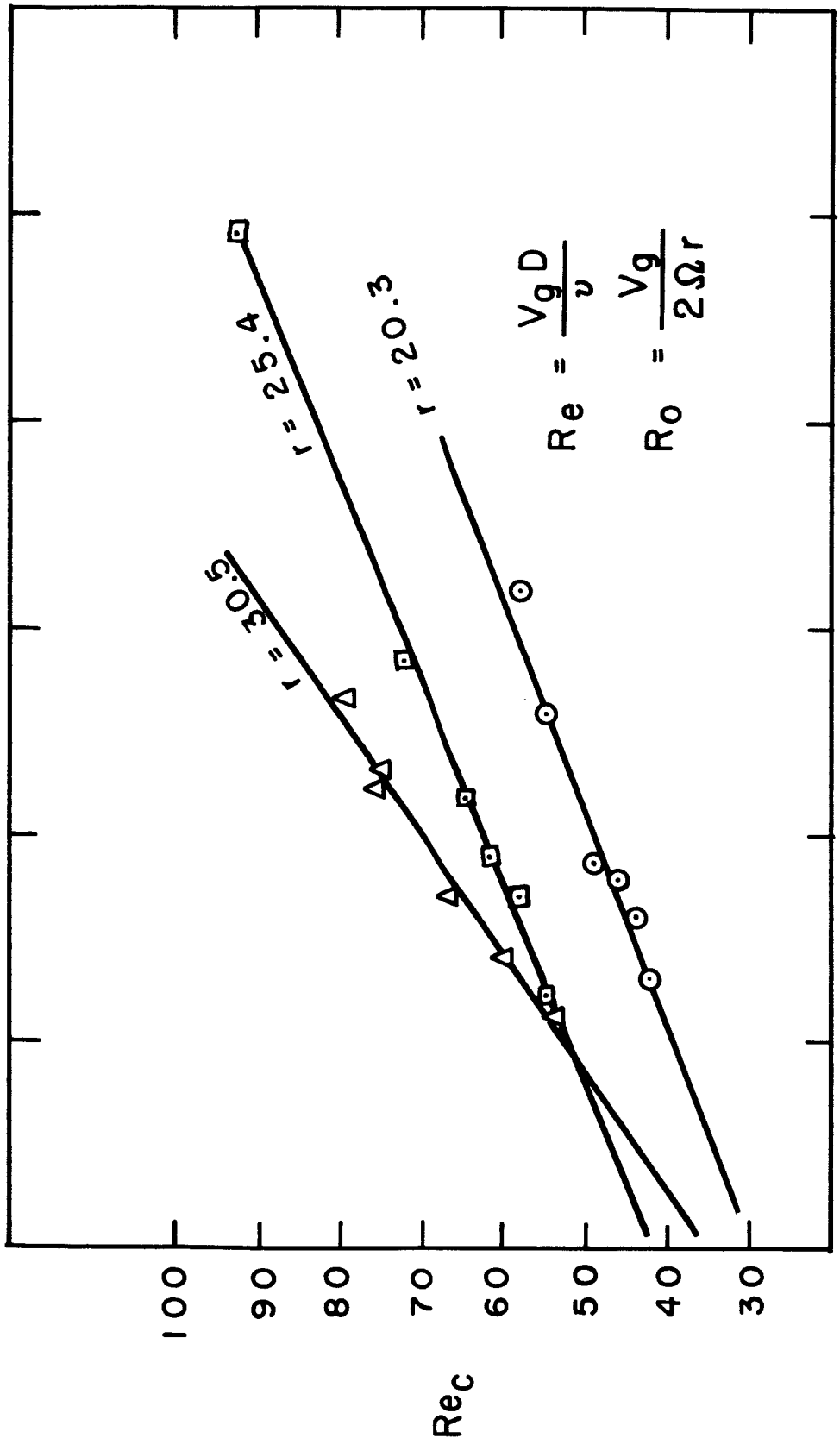

Figure 4.2 Critical Reynolds number versus Rossby number based on the measured geostrophic velocity

IV.3 Type II Critical Reynolds Number based on Geostrophic Velocity and Boundary Layer Thickness

To further refine the Reynolds number, the boundary layer thickness for each of the eighteen sets of parameters was measured as described in section III.5. The new value of the Reynolds number

$$Re = V_g \delta / \nu$$

was computed for each run, and plotted against the value of the Rossby number previously computed using geostrophic velocity. The results are shown in figure 4.3. The points from all three measuring stations now appear to form a reasonably straight line. A least-squares linear regression line was calculated using standard statistical methods (Hoel, [19]), and found to be:

$$Re_{IIc} = 56.3 + 116.8\ Ro$$

The measurements of the geostrophic velocity are considered to have an accuracy of $\pm$ 0.5 cm sec^{-1}, and the measurements of boundary layer thickness were found to be repeatable to within $\pm$ 0.004 cm, hence the minimum critical Reynolds number of Type II waves is taken to be

$$Re_{IIc} = 56.3 \pm 2.0$$

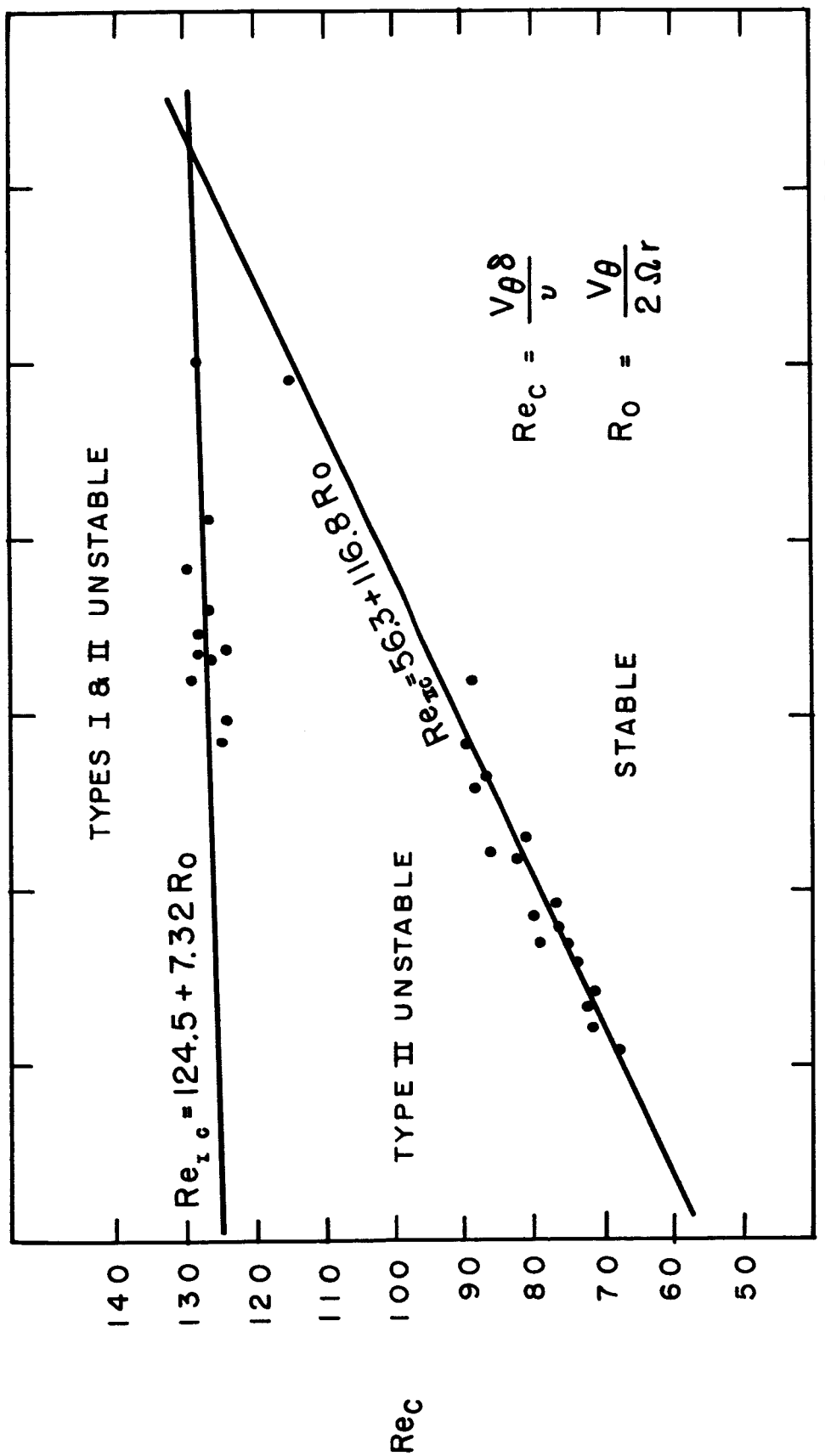

Figure 4.3 Critical Reynolds number versus Rossby number based on the measured geostrophic velocity and measured boundary layer thickness

IV.4 The Boundary Layer Profile

To determine the changes in boundary layer profile, if any, with mass flow rate; a series of vertical profiles of radial velocity through the boundary layer were made at varying S for a fixed Ω. Figure 4.4 shows one of these results. The boundary layer was found to decrease in thickness with increasing mass flow at a fixed r and Ω up to approximately the critical Reynolds number. Increasing S beyond this point did not change the thickness noticeably. Attempts to correlate the ratio of δ to D with Reynolds number, Rossby number, or Ekman number were unsuccessful; thus the boundary layer thickness remains an undetermined function of Re, Ro.

That the instability does indeed originate in the boundary layer is shown quite clearly by profiles taken just after the onset of instability. Figure 4.5 shows profiles of radial and tangential velocity with the instability oscillations confined to the boundary layer. The oscillations seem to reach a maximum in the radial velocity profile, and at a somewhat higher point in the tangential profile. It is difficult to assess the height of maximum amplitude in the tangential velocity profile.

IV.5 Critical Reynolds Number of the Type I Instability

As discussed in section III.6, a second instability mechanism seems to occur at a higher Reynolds number. The value of Reynolds number at which this change occurred was not determined as before; rather, the geostrophic velocity was determined and the boundary

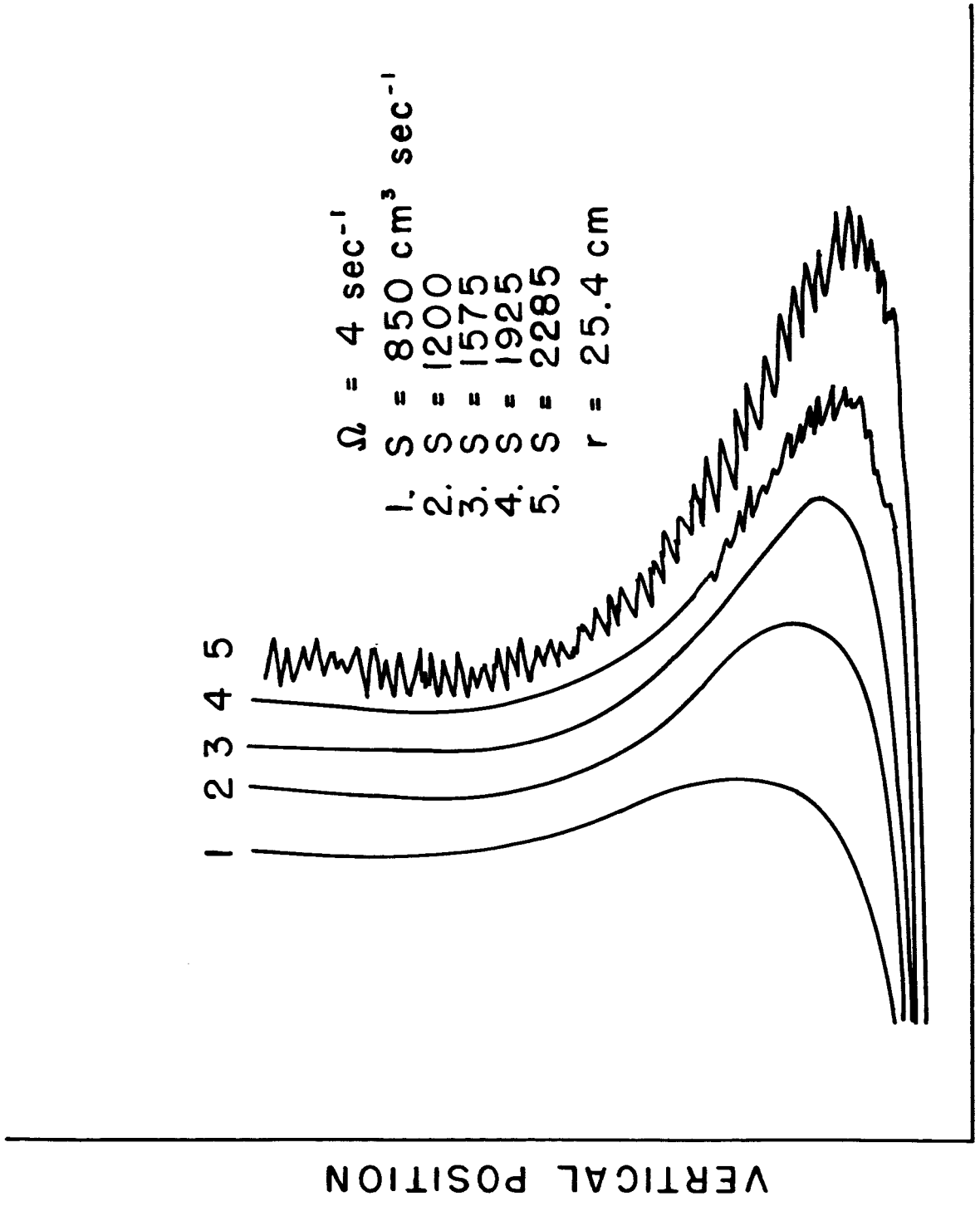

Figure 4.4 The boundary layer thickness as a function of the mass flow rate

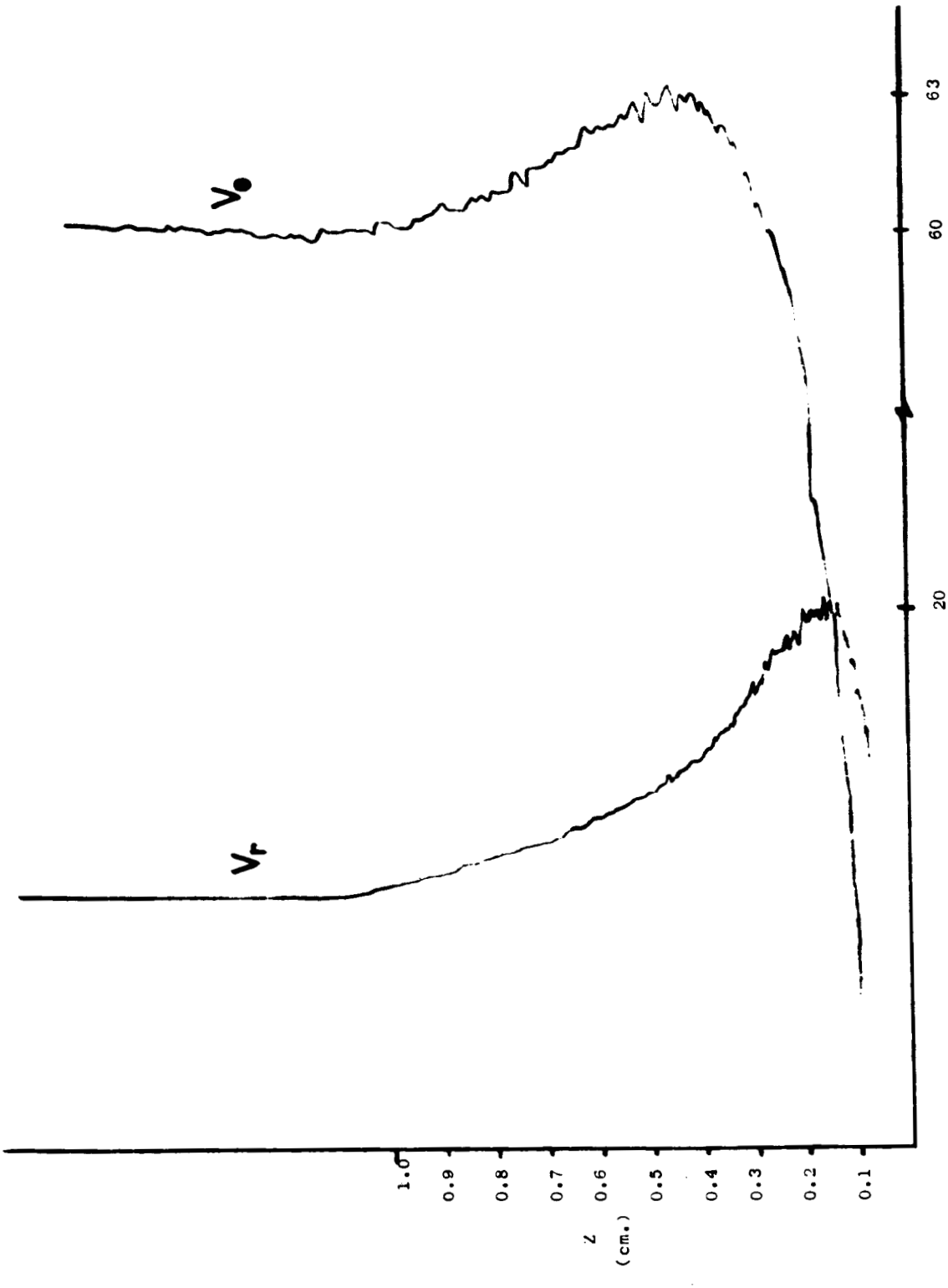

Figure 4.5 Profiles of the radial and tangential velocity components as functions of height with the instability oscillations confined to the boundary layer

layer thickness was taken to be the same as had been previously measured at lower Re. This assumption was based on the results of the previous section, and is believed to be fairly accurate. These results are shown in figure 4.3. The actual boundary layer thickness would tend to be equal to or less than the value used in the computation of the Reynolds number, since S is greater than before; hence the computed values of Re may be on the high side. A linear regression based on ten points for the Type I instability yielded

$$Re = 124.5 + 7.32\ Ro$$

The scatter of the points about the regression line is such that the computed value of the slope may not be entirely significant. It was not felt necessary to be as precise with this instability as with the previous because of the very close agreement with Fallers results.

IV.6 Wave Length and Orientation of the Type II

The wave length and orientation of the waves were determined as described in section III.8. Fifteen measurements were made of Type II waves; the non-dimensional wavelength λ/D was found to vary from 25.0 to 33.0 with a mean of 27.8 and a standard deviation of 2.0. To compare these values with those computed theoretically by Stern [7], the Taylor number Ta was computed for each run, and the ratio of the non-dimensional wavelength to the one-fourth power of the Taylor number. Stern predicted a relationship of the form

$$\lambda = K\, Ta^{\frac{1}{4}}\, D$$

where K is a constant approximately equal to 2π. A statistical analysis of the fifteen measurements showed a mean value of the constant of 5.98 with a standard deviation of 1.05. This result is not as significant as it might first appear. Stern's relationship, if the Taylor number is conventionally defined as:

$$Ta = \Omega h^2/\nu$$

reduces to

$$\lambda = CD^{\frac{1}{2}}$$

which states that the wavelength is proportional to the square root of the Ekman depth. The standard deviation when the wavelength was related to the Ekman depth was 7.2% of the mean; when related to the square root of the Ekman depth the deviation is 17.5% of the mean. It would therefore appear that these waves are not the type described by Stern.

The angle ε, measured between the wavefront and the tangential direction, varied from 0 degrees to eight degrees to the right of the basic flow (this is considered a negative angle), with larger angles generally associated with higher rotation rates.

The average phase velocity of these waves was $\bar{C} = 7.72$ cm sec^{-1} directed radially inward, with the highest phase velocities associated with the lowest rotation rates. This corresponds to approximately 16% of the geostrophic velocity.

IV.7 Wave Length and Orientation of the Type I

The Type I waves, occurring at an average Reynolds number of 127 with an average Rossby number of 0.33, had a nearly constant angle of orientation; $\bar{\varepsilon}$ was found to be + 14.6 degrees with a standard deviation of 0.8 degrees.

The non-dimensional wavelength λ/D had a mean of 11.8 with a standard deviation of 0.46. The phase velocity normal to the wave-front had a mean of 2.44 cm sec^{-1}, which corresponds to approximately 3.4% of the geostrophic velocity. Once again there was a tendency for the highest phase velocities to be associated with the lowest rotation rates.

IV.8 The Geostrophic Velocity as a Function of Height

The theory predicts that the geostrophic flow in the interior regions away from the boundaries will be independent of height. To test this, several vertical profiles of tangential velocity were made at different radii from the lower boundary to the middle of the tank. At r = 25.4 cm the velocity was virtually constant above a non-dimensional height $Z' = 3\pi$. At a radius r = 30.5 cm the velocity showed non-periodic variations of two to three percent; these are believed to be effects of the outer transition region.

IV.9 The Geostrophic Velocity as a Function of Radius

The geostrophic velocity as a function of radius was measured as described in section III.3. Figure 4.6 is a plot of a typical

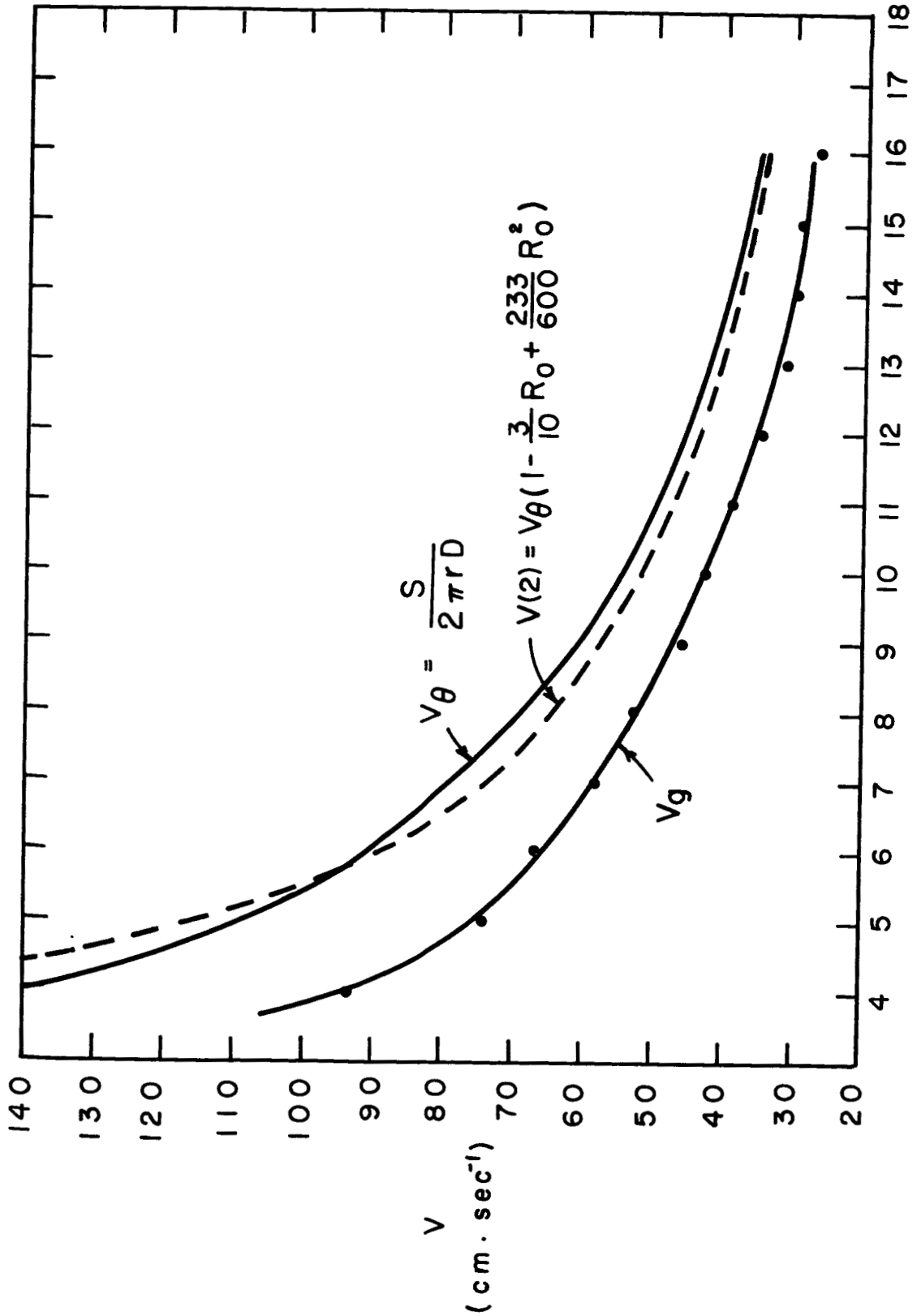

Figure 4.6 Profile of the geostrophic velocity as a function of the radial position

$V_g(r)$ profile. The geostrophic velocity was found to be in all cases less than the tangential velocity. The ratio of geostrophic to tangential velocity had a minimum value at minimum radius, and increased monotonically with increasing radius. The second order tangential velocity V(2) was calculated according to Faller's [9] work, and is shown on the same plot. The Rossby number correction does not markedly alter the theoretical profile; however, the correction is largest in the $7 < r < 9$ inch range, and the $V_g/V(2)$ ratio hits its maximum at this point.

IV.10 The Vertical Boundary Layers

Since the rotating tank was essentially bounded by vertical walls at the hub and outer edge, it would be expected that vertical boundary layers would form at these boundaries. The boundary layer around the hub is a thin viscous layer which shows up quite clearly on the $V_g(r)$ profiles (see figure 3.2). The zero order approximation to its width was found by Faller to be:

$$W(r) = (\nu H/\Omega)^{1/3}$$

which is approximately 0.5 cm for $\Omega = 60$ rpm. The measured width was 0.4 cm.

The outer transition region is vastly more complicated, for by observation it is wider by a factor of ten or more. Faller reasoned that the width of the outer layer must be sufficient to preclude centrifugal instability; computations based on this yield a width

of the outer transition region of the order of five cm. The same analysis, however, should hold for the inner hub where the width would have to be greater since the velocities are higher. By observation this is not the case.

Some effects of the outer transition region, in the form of non-periodic velocity fluctuations, were noticed with a hot wire in the boundary layer at r = 30.5 cm at Reynolds numbers below critical and rotational rates below 60 rpm. This would imply that the width of the transition region is approximately (R-30.5) cm or 15 cm with V_g = 65 cm sec^{-1}. Neither the viscous analysis nor the centrifugal instability analysis come close to predicting this width, and it is felt that there must be some other mechanism dominant.

IV.11 Turbulence

Figure 4.7 shows oscilloscope photographs of the hot wire voltage as a function of increasing S, hence increasing Re, in the unstable region. The time and amplitude scales for all the photographs are the same. Patches of high frequency appear first on the wave peaks; then as Re is increased the high frequency increases in amplitude and spatial extent, finally becoming periodic bursts of turbulence. Increasing Re even further results in the trace becoming fully turbulent. No ordered pattern was noticed in the onset of turbulence. On some runs, turbulence could be detected at Reynolds numbers below 200; on others none was noticed up to Reynolds numbers as high as 350. The pictures do, however, give a qualitative feeling for how the turbulence is generated.

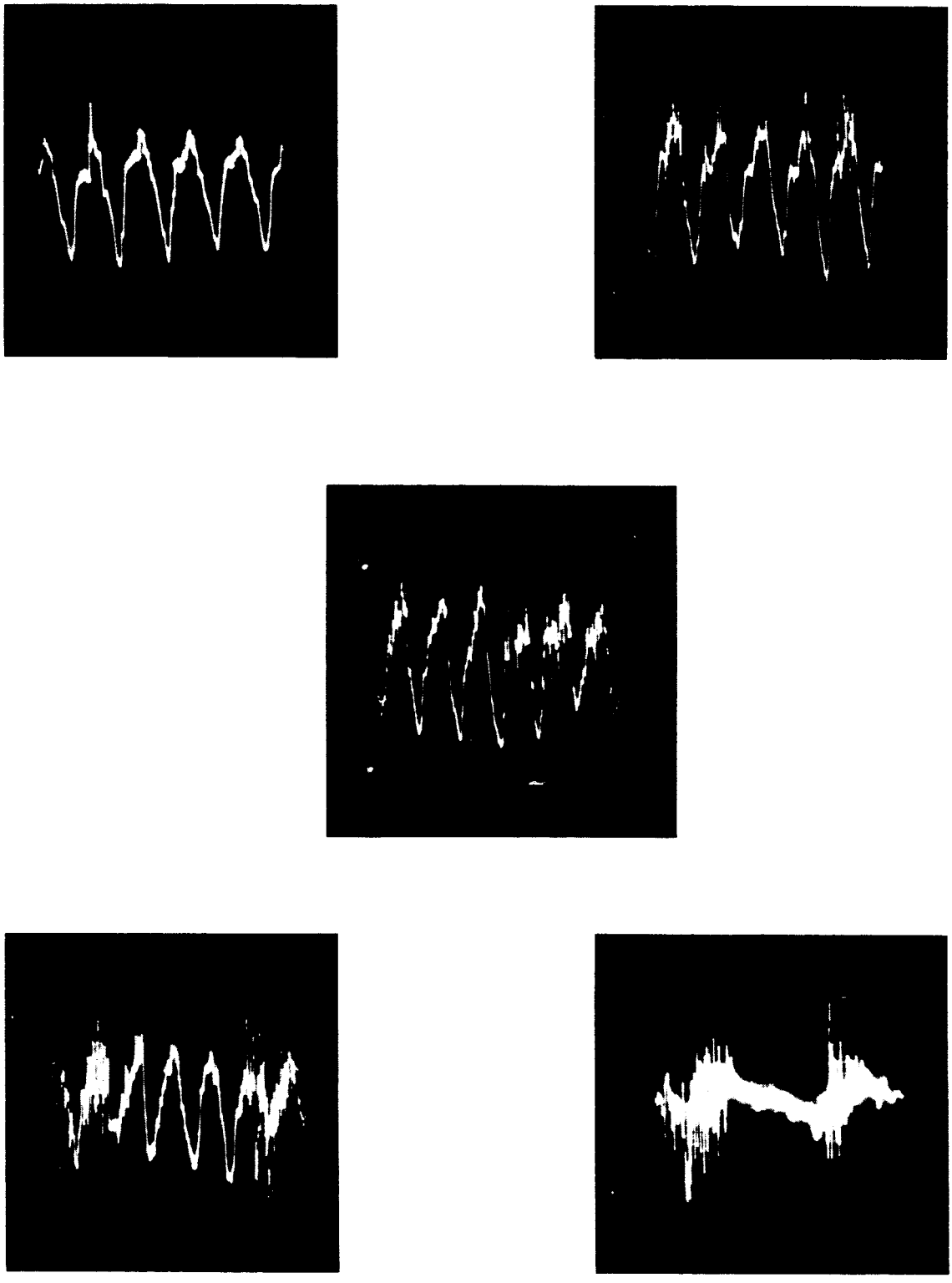

Figure 4.7 Oscilloscope photographs of the hot wire voltage as a function of the Reynolds number showing the onset of turbulence

CHAPTER V

DISCUSSION

V.1 A Theory on Tank Circulation

The computations of Re and Ro based on mass flow are based on the assumption that the entire radial transport occurs in the boundary layer. Consider the effect, however, of having even a very small ageostrophic component to the interior flow. This would act to radially transport mass across a large vertical section. For example, an interior flow varying one degree from the tangential direction at a radius of 25 cm would have a radial mass transport of $21|V_g|\,cm^3 sec^{-1}$. Using typical values of V_g = 60 cm sec^{-1} and S = 1745 cm^3 sec^{-1}, it is seen that even this small deviation from geostrophy could provide a mass transport of 1260 cm^3 sec^{-1}, or 73% of the total! From continuity considerations, the net mass flow across any section must be a constant; therefore any transport accomplished in the interior must be felt as a corresponding increase or decrease in the boundary layer transport.

If the radial component of boundary layer velocity is assumed to have the basic Ekman profile with a characteristic depth different than the Ekman depth, and to be in equilibrium with the measured geostrophic velocity above it:

$$V_r = V_g\, e^{-z/\delta} \sin^{z/\delta}$$

This may be integrated over a vertical section of radius r:

$$2(2\pi r)\, V_g \delta \int_0^a e^{-z/\delta} \sin(z/\delta)\, d(z/\delta) = S^*$$

to obtain the mass transport of the boundary layer. The difference between this value and the mass transport S as measured by the flowmeter is a measure of the departure from geostrophy. Direct integration yields:

$$S^* = 2\pi r\, \delta\, V_g$$

S^* and the ratio S^*/S were computed for each of the observations of Type II instability. At a radius of 20.3 cm, S^* was always greater than S, with an average value of the ratio of 1.29. At a radius of 25.4 cm S^* was always greater, but the ratio varied from 1.25 at Ro = 0.491 to 1.10 at Ro = 0.122. At a radius of 30.5 cm, S^* was always less than S, with the ratio varying from 0.885 at Ro = 0.226 to 0.993 at Ro = 0.113. Thus it is seen that the transport through the boundary layer is less than the net transport at large radius, and greater than the net transport at small radius. The boundary layer transport seems to approach the net transport as a limit from both directions as the Rossby number approaches zero at some radius $25.4 \leq r \leq 30.5$. Figure 5.1 is an intuitive model of an interior circulation which would satisfy the criteria developed here.

V.2 Inertial Waves Associated with the Type II Instability

Consider a time dependent perturbation equation for the

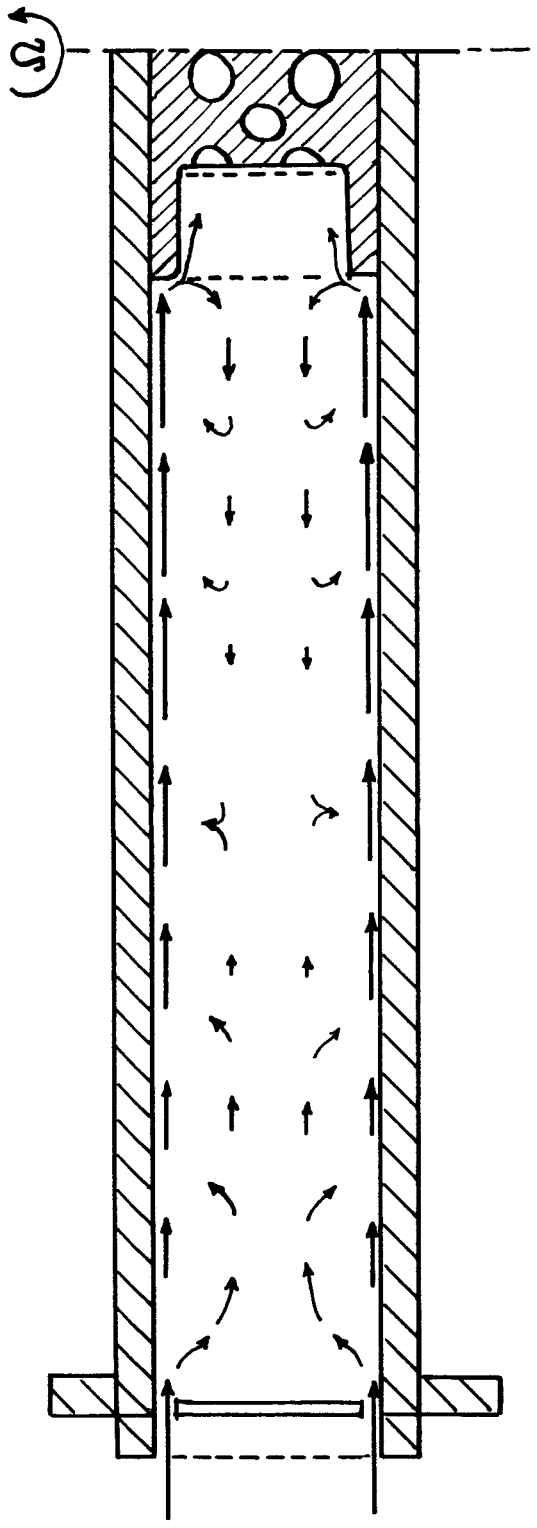

Figure 5.1 An intuitive model of the rotating tank circulation

boundary layer, which assumes small Rossby number, small perturbation Rossby number, and large Taylor number:

$$\frac{\partial \bar{V}}{\partial t} + 2\bar{\Omega} \times V = -\nabla(P/\delta)$$

Operating on this equation with CURL to eliminate the pressure, and assuming a periodic solution of the form

$$\{u, v, w\} = \{\hat{u}, \hat{v}, \hat{w}\} \exp\left[i\,(kx + ly + mz - \omega t)\right]$$

yields three linear homogeneous algebraic equations in three unknowns. The requirement that the determinant of the matrix of coefficients vanish for the existence of a non-trivial solution yields:

$$\left[\frac{2\Omega i m}{\omega}\right]\left[\left(\frac{2\Omega i m}{\omega}\right)^2 + (k^2 + \ell^2 + m^2)\right] = 0$$

which may be satisfied either by $m \equiv 0$ or

$$m = \pm i \sqrt{\frac{k^2 + \ell^2}{1 - 4\Omega^2/\omega^2}}$$

Three possibilities now exist: (1) $\omega < 2\Omega$; the radical is imaginary and the wave has a vertical wave number; (2) $\omega > 2\Omega$; the radical is real and the wave has an exponential vertical decay (the requirement that the wave remain finite for large Z eliminates the choice of the minus sign in front of the radical in this case), and (3) $\omega = 2\Omega$; in which the radical becomes infinite and the choice

$m \equiv 0$ must be taken. This is a purely inertial wave which is independent of height.

The Type II instability has been shown to originate in the boundary layer, and it generally occurs with $\omega > 2\Omega$. As the amplitude increases, however, an inertial response seems to be stimulated; the frequency shifts downward such that ω is less than 2Ω and the wave is found all the way through the interior region. Vertical profiles of the horizontal velocity components at Reynolds numbers slightly above critical showed the perturbations extending without noticable attenuation of amplitude up through the geostrophic region. Figure 5.2 shows a typical profile.

There seemed to be a tendency for the frequency shift to occur more rapidly after the onset of instability at higher rotation rates; this would explain why the computed phase velocities of the waves tended to be higher at lower rotation rates.

V.3 The Type I Instability

The change in the character of the instability signal was drastic when the hot wire was 3 mm from the boundary, and not

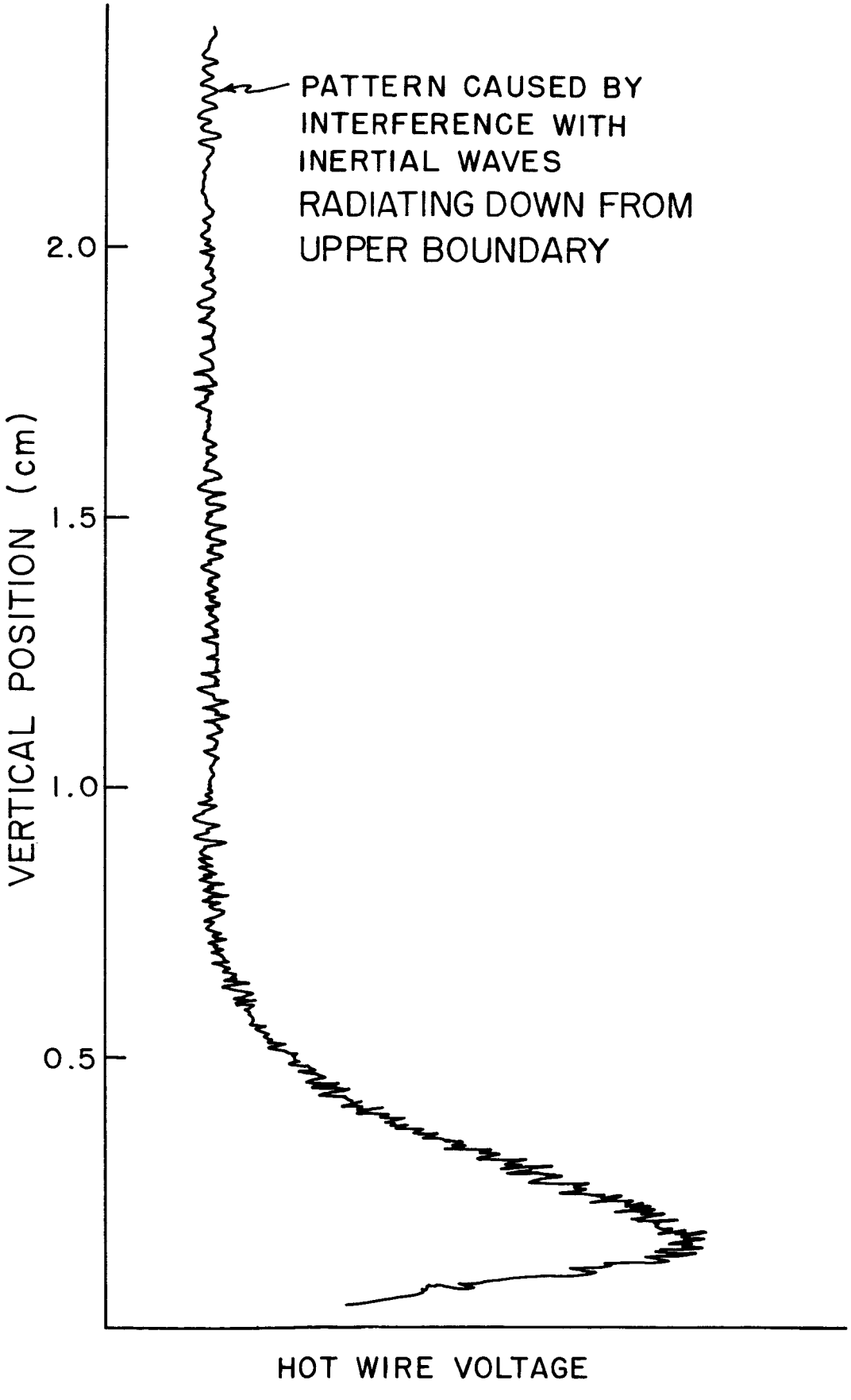

Figure 5.2 The radial velocity as a function of height showing the inertial oscillations extending through the interior geostrophic region

detectable when the wire was at 6 mm. Thus, at least at its onset the Type I instability seemed to be confined to the boundary layer. Since the Type II always occurred with the Type I, and the first manifestations of the onset of turbulence were generally noticed at only slightly higher Reynolds number; the vertical development, if any, of the Type I waves was not investigated.

V.4 Forcing the Instability

In an attempt to lock the instability signal onto a single clear frequency to simplify the investigation of wave parameters and to allow an investigation of the stability as a function of frequency; a chopping mechanism was introduced into the air line from the vacuum cleaner to the tank which put approximately sinusoidal pressure disturbances into the tank. This did not alter the frequency of the Type II instability at all; the observed frequency was the same with or without the chopper operating.

The introduction of a vertical rod at a small radius was found to increase the instability signal for a given S and Ω. To ensure that this rod did not distort the signal, four rods, having diameters of 0.100 cm, 0.156 cm, 0.273 cm, and 0.356 cm were tested at the same S and Ω. The frequency of the observed instability was the same in each case. The 0.100 cm rod was used to stimulate the instability for all phase and orientation measurements.

These results would tend to confirm Lilly's [13] assertation that energy is abstracted from the mean flow to support the

disturbance growth only through the Coriolis term and to indicate that the mechanism discussed by Stern [7] in which the quasi-hydrostatic transmission of pressure fluctuations couples the boundary and the interior, is not important here.

V.5 Atmospheric Considerations

Considering a typical value of atmospheric eddy viscosity of $K = 2 \times 10^{5}$ cm^{2} sec^{-1} and a value of the Coriolis parameter of $f = 10^{-4}$ sec^{-1}, it is seen that the Ekman layer depth is 440 meters, or 1443 feet. Yet, aircraft at altitudes of several thousand feet over water have reported periodicity in humidity measurements which they attributed to the Ekman layer.

The critical value for Type II instability would be reached under these conditions at a wind velocity of 270 cm sec^{-1} or less than six knots. It is possible, therefore, that the aircraft are in reality sensing inertial waves radiated from the unstable boundary layer. Based on experimental evidence, it would be expected that these fluctuations would have a wavelength on the order of 12 km; however, aircraft data for comparison with this figure are not presently available.

CHAPTER VI

RECOMMENDATIONS

VI.1 Further Experimental Work

Although the basic wave parameters have been measured in this experiment, instrumentation and tank design limitations have left many unanswered questions.

Stuart [6] in 1955 first described the instability waves as horizontal roll vortices superimposed on the basic flow, but a detailed experimental investigation of the structure of these vortices has never been carried out. It would be interesting to determine and compare the detailed structure of the two types of instability.

Another suggested area of fruitful research is the analysis of the frequency spectrum of the instability as a function of Reynolds number. There seemed to be a tendency for ω to increase with increasing Re until ω approached 2Ω, at which time a subharmonic would become dominant. This was never investigated because the frequencies involved were so low; however, the use of a tape recorder with a wide speed range would bring these frequencies up to the operating range of a wave analyzer.

The undetermined question conerning the width of the outer transition region would certainly benefit from more detailed measurements at large radius. These might well include radial profiles of the velocity components at a variety of S and Ω to

determine if the width is a function of height as well as the other parameters.

The critical Reynolds number of the onset of turbulence, the mechanism by which it is generated, its behavior as a function of Re and Ro, and its statistical character are all areas where no quantitative work has been done. The proven compatibility of hot wire anemometers with turbulence studies suggests that an apparatus of the type which was used here would be ideal for such studies.

VI.2 Recommended Equipment Modifications

While operating the tank over a period of approximately one year, several limitations and disadvantages of the design were noticed which should be eliminated before further studies are initiated.

The use of plexiglass for the upper and lower plates allows the observation of smoke etc. inside the tank, but makes these surfaces subject to deformation with time and stress. The initial plate spacing of 3.00 inches was found to be off by $\pm$ 0.2 inches after a few months, and it was necessary to bolt spacers around the outer rim to bring the spacing back to the design value.

The three inch spacing between the plates is considered less that ideal. At 16 rpm, the center of the tank is only 12 Ekman depths from the boundaries.

It is felt that the diameter of the tank should be increased.

The transition zone extends in for approximately 15 cm, and the curvature becomes rather large inside a radius of about 20 cm. Data from these experiments indicated that the measured boundary layer thickness and the geostrophic velocity approach their theoretical values only in the range $30 \geq r \geq 25$ for small Rossby number. Extending the radius of the tank to 75 cm would extend this range to approximately 35 cm.

A more ideal rotating tank is envisioned as being 1.5 meters in diameter, with aluminum or steel upper and lower plates spaced 12 cm apart; and having a slip ring block containing 12 or more rings mounted on the bottom of the tank with the wires running out through the hollow shaft. This would allow 4 rings for a double hot wire probe, 2 for each of two positioning drives, and 2 for each of two position potentiometers. Undoubtedly, new instrumentation will generate a requirement for additional rings; the figure twelve is considered only as a minimum.

Having the rings on the bottom would eliminate the present alignment problem and the need for the overhead framework.

The ideal traversing mechanism for this tank is considered to be one which would allow radial traversing of a probe at any height, and allow the change of position of two wires relative to each other while the tank is in motion. Unfortunately, a working design for this ideal has not been developed.

BIBLIOGRAPHY

1. Sverdrup, H. U., M. W. Johnson and R. H. Fleming: The Oceans. Prentice-Hall, Inc., 1942.

2. Ekman, V. W.: "On the influence of the earth's rotation on ocean currents". Arkiv. f. Matem., Astr. o. Fysik, Stockholm, Bd. 2, No. 11, 53 pp.

3. Schlichting, H.: Boundary Layer Theory, 4th Ed. McGraw-Hill Book Co., Inc., 1960.

4. Theodorsen, T. and A. Regier: "Experiments on drag of revolving discs, cylinders, and streamline rods at high speeds". NACA Report No. 793, 1947.

5. Smith, N. H.: "Exploratory investigation of laminar boundary layer oscillations on a rotating disc". NACA Tech. Note 1227, 1947.

6. Gregory, N., J. T. Stuart and W. S. Walker: "On the stability of three dimensional boundary layers with application to the flow due to a rotating disc". Phil. Tran. A 248, 155-199, 1955.

7. Stern, M. E.: "Instability of Ekman flow at large Taylor number". Tellus, 12, 399-417, 1960.

8. Arons, A. B., A. P. Ingersoll and T. Green: "Experimentally observed instability of a laminar Ekman flow in a rotating basin". Tellus, 13, 31-39, 1961.

9. Faller, A. J.: "The development of fluid model analogues of atmospheric circulations". W.H.O.I. Final Report, Contract AF19(604)-4982, GRD, AFCRL, 1962.

10. Fultz, D.: "Non-dimensional equations and modeling criteria for the atmosphere". J. Meteor., 8, 262-267, 1951.

11. Faller, A. J.: "An experimental study of the instability of the laminar Ekman boundary layer". J. Fluid Mech., 15, 560-576, 1963.

12. Barcilon, V.: "Stability of a non-divergent Ekman layer". Tellus, 17, 53-68, 1965.

13. Lilly, D. K.: "On the instability of Ekman boundary flow". J. Atmos. Res., 23, (submitted for publication) 1966.

14. Faller, A. J. and R. E. Kaylor: "A numerical study of the instability of the laminar Ekman boundary layer". J. Atmos. Res., 23, (submitted for publication) 1966.

15. Faller, A. J. and R. E. Kaylor: "Investigations of stability and transition in rotating boundary layers". Tech. Note BN-427, Institute for Fluid Dynamics and Applied Mathematics, University of Maryland, 1965.

16. Roshko, A.: "On the development of turbulent wakes from vortex streets". NACA TR 1191, 1954.

17. Rosenhead, L.: Laminar Boundary Layers. Oxford University Press, 1963.

18. Wills, J. A. B.: "The correction of hot wire readings for proximity to a solid boundary". J. Fluid Mech., 12, (3), p 388.

19. Hoel, P. G.: Introduction to Mathematical Statistics, 2nd Ed. John Wiley and Sons, Inc., 1956.

20. Corrsin, S.: "Turbulence, Experimental Methods". Handbuch der Physik, Volume VII/2, pp 524-590.

21. Collis, D. C. and M. J. Williams: "Two-dimensional convection from heated wires at low Reynolds numbers". J. Fluid Mech., 6, p. 357, 1959.

22. Flow Corporation: "Constant current, constant temperature, and constant resistance ratio hot wire anemometer circuits". Bulletin No. 40, Flow Corporation, Cambridge, Mass.

23. Browand, F. K.: "An experimental investigation of the instability of an incompressible, separated shear layer". ASRL TR 92-4, 1965.

24. Bridgeman, P. W.: Dimensional Analysis. Yale University Press, 1937.

APPENDIX A

THEORY, CONSTRUCTION, CALIBRATION AND OPERATION OF HOT WIRES

A.1 Basic Hot Wire Theory

The following is a simplified development of hot wire theory presented for basic understanding; a more complete development is given by Corrsin [20].

Consider the application of the First Law of Thermodynamics to a cylindrical wire of diameter d, length ℓ, and temperature T; suspended perpendicular to a uniform flow of fluid of velocity U and temperature T_a:

$$\frac{dE}{dt} = \frac{dQ}{dt} - \frac{dW}{dt} \tag{1}$$

$$\frac{dE}{dt} = \rho \frac{\pi d^2}{4} C_p \ell \frac{dT}{dt} = \text{change of internal energy}$$

$$\frac{dW}{dt} = - I^2R = \text{Joule heating}$$

$$\frac{dQ}{dt} = - h\pi d\ell(T - T_a) = \text{transfer of heat}$$

across the surface area of the wire, with h the heat transfer coefficient, sometimes called the "film coefficient". The equation as it stands cannot be evaluated directly, however, because h is an unknown function not only of the flow velocity U and the wire geometry, but also of the fluid properties:

$$h = f(u, d, C_p, k, \mu, \rho) \qquad (2)$$

where U = velocity of flow

d = wire diameter

μ = fluid viscosity

ρ = fluid density

C_p = fluid specific heat at constant pressure

k = fluid thermal conductivity

Using the π-Theorem of dimensional analysis (Bridgeman [24]), these seven unknowns can be arranged into three dimensionless parameters:

$Nu = \frac{dh}{k}$, The Nusselt number, a dimensionless heat transfer coefficient

$Re = \frac{Ud\rho}{\mu}$, The Reynolds number, a ratio of viscous to inertial forces

$Pr = \frac{\mu C_p}{k}$ The Prandtl number, a ratio of momentum diffusivity to heat diffusivity in the fluid.

For air, the Prandtl number is essentially constant, and the relationship reduces to:

$$Nu = Nu\,(Re) \qquad (3)$$

This relationship has been found by Collis and Williams [21] to fit the following empirical equation for a fixed overheat ratio $(T - T_a)/T_a$

$$Nu = A_1 + B_1\, Re^m \qquad (4)$$

where A_1, B_1, and m are constant over fixed Reynolds number ranges, with m = 0.45 over the range of interest of this paper.

This may be written as

$$h = \frac{k}{d}\,(A_1 + B_1\,Re^{0.45}) \tag{5}$$

Thus,

$$\frac{dQ}{dt} = -\pi \ell k\,(A_1 + B_1\,Re^{0.45})(T - T_a) \tag{6}$$

If the resistance is taken as a function of the temperature only, and expanded in a power series:

$$R = R_a\,[1 + a_1(T - T_a) + a_2(T - T_a)^2 + \ldots] \tag{7}$$

utilizing the first two terms yields:

$$T - T_a = \frac{R - R_a}{a_1 R_a} \tag{8}$$

making this substitution, the First Law may be written in the form:

$$\rho C_v \frac{\pi d^2}{4}\,\ell\,\frac{dT}{dt} = I^2R - \frac{\pi \ell k}{a_1 R_a}(A_1 + B_1[d/\nu]^{0.45}\,U^{0.45})(R - R_a) \tag{9}$$

In this equation, the term on the left represents the thermal inertia of the wire; the first term on the right is the power supplied, and the second represents the heat carried away by forced convection. Assuming a flow of velocity U = 50 cm sec^{-1}, a wire length of 1 cm, a wire diameter of 1.6 X 10^{-4} inches, and evaluating fluid properties

at ambient temperature; each of these terms may be evaluated. The two on the right are found to be of order 10^{-2} cal sec^{-1}, while the term on the left is of order 10^{-8} dR/dt cal sec^{-1}. Thus for even large amplitude high frequency response, steady state heat loss calibrations can be used in calculating the dynamic response of the wire. Assuming the parameters for any given wire remain constant, and that the fluid parameters are constant over the operating range, the hot wire response equation may be written as

$$\frac{I^2R}{R - R_a} = A + BU^{0.45} \qquad (10)$$

A and B are now constants for any given calibration, but may vary from wire to wire or time to time because of different contact resistances in soldering, the carrying away of heat from the wire by the supporting needles, the accumulation of dust on the wire etc.

A.2 Hot Wire Probe Construction

The function of a hot wire probe is merely to provide supports upon which the sensing wire may be mounted, while introducing the least possible disturbance into the flow. Any material which is convenient, and any shape which serves to put the wire in the desired position may be used. Small ordinary sewing needles, such as number 12, make ideal wire supports since they present a minimum obstruction to the flow.

The single wire probes used in this series of experiments were

constructed of a 0.10 inch diameter stainless steel tube with two needles mounted on one end. One needle was held inside the tube and insulated from the tube by means of an epoxy type cement. A wire soldered to this needle and running through the tube acted as electrical conductor for this point. The other needle was soldered to the side of the tube, with the tube itself acting as a conductor. All the single wire probes utilized a 3/16 inch needle point spacing. After the needles were in place, a collar of epoxy was built up around the end of the tube and the base of the two needles. This was then machined to give the probe a smooth profile.

Both double wire probes used were constructed by mounting needles in a plexiglass plug, which was designed to fit into the holes on the top of the rotating tank with the underside of the plug flush with the inside of the tank top. Stranded copper wires were soldered to the needles using stainless steel flux, and the needles were then held in place in the plexiglass by epoxy. When it was desireable to bend a needle, as in the construction of the double vertical wire proge (figure 2.8), the needle was heated first to prevent it from breaking.

A.3 Mounting Hot Wire Filaments

The key to a well soldered joint between the needle points and the wire is having the needle points well tinned before the mounting operation is started. Since sewing needles are generally stainless steel, a good stainless steel flux should be used, and then neutralized

after the tinning is completed.

The wire used as filaments was a 0.00016 inch diameter platinum wire with 10% Rhodium for added strength. As purchased, the wire had a diameter of 0.002 inch, having an outer layer of silver which must be removed before the wire is used as a sensor. Two different techniques may be employed here:

The first method removes the outer coating of the wire before it is soldered to the probe. A 70 normal nitric acid solution etches the platinum clean in about five minutes. Soldering the etched wire to the needle points is a delicate operation requiring patience, a steady hand, patience, the proper equipment, and patience. The proper equipment consists of: (1) a micromanipulator to hold the hot wire probe, capable of moving the needle points by fine degrees about each of its three axes; and having a yoke or fork from which the wire may be suspended; (2) a good optical system, since the etched wire is virtually invisible to the naked eye; and (3) a micro-miniature soldering iron with a variable heat control (figure A.1).

In mounting the wire, a small weight must first be attached to each end of a $1\frac{1}{2}$ - 2 inch section of the etched wire. This is most easily accomplished by putting a small drop of lacquer on the weight, and placing the end of the wire in the lacquer. The weighted wire is then hung across the fork, with the free hanging weights keeping the proper tension on the wire while it is soldered. The probe points are then manipulated until the wire is perfectly aligned with

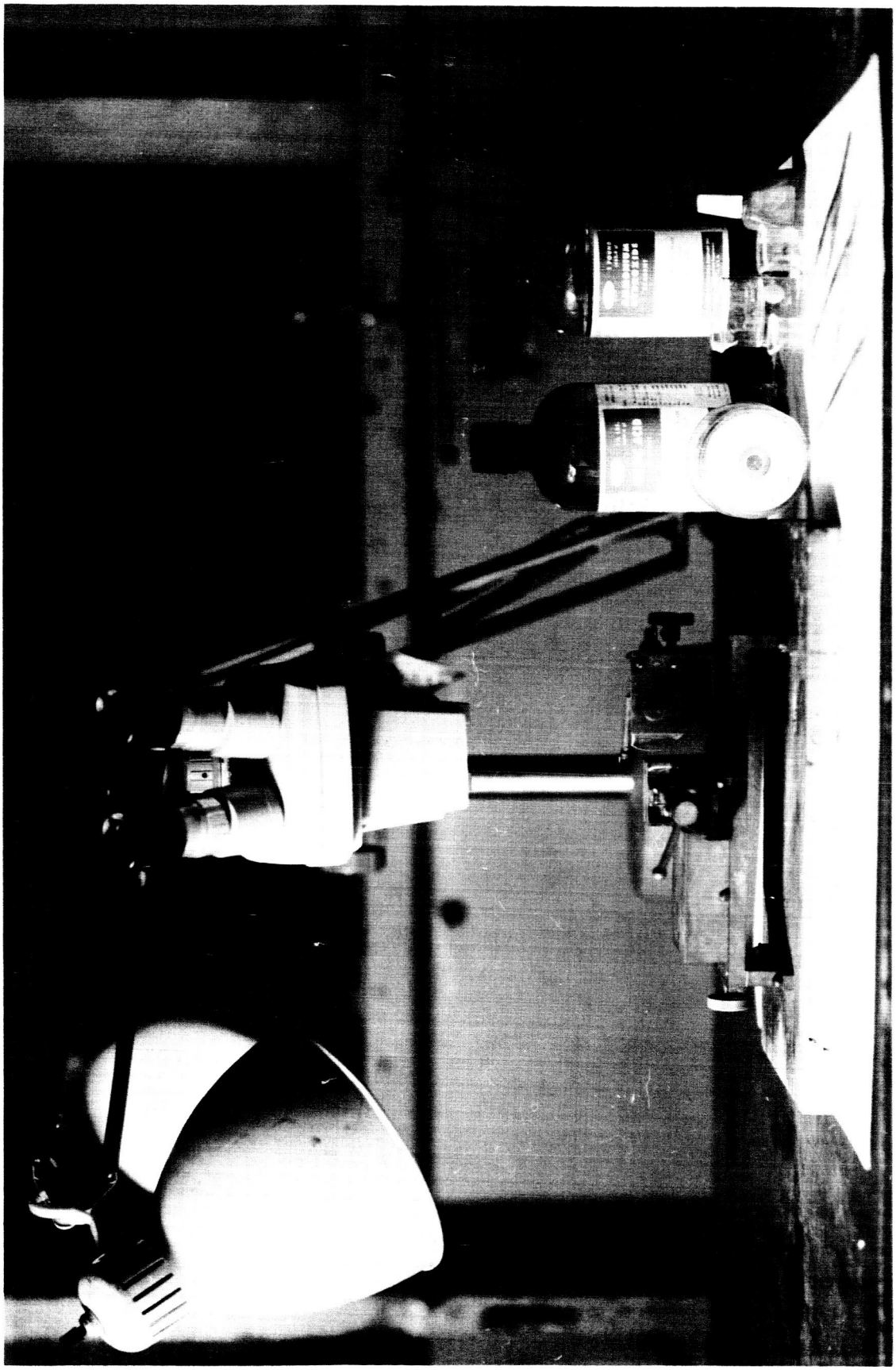

Figure A.1 Typical equipment used in hot wire construction

$$f = \frac{0.212}{d} U - \frac{4.5\nu}{d^2} \quad (50 < Re_r < 150) \qquad (11)$$

In practice, the shedding frequency was determined by the use of an oscillator to draw Lissajous figures on an oscilloscope. The hot wire output was fed back through the slip rings of the rotating tank to the potentiometer, so that all of the same components were used in calibration as in operation. For each change of velocity through the wind tunnel, the hot wire voltage, the cylinder diameter, and the shedding frequency were recorded.

Since the calibration of a given hot wire may change daily (Browand [23], it is necessary to calibrate both before and after each session of data taking. To simplify the procedure, and cut down on the time required for calibration, a multi-element graph was developed (figure A.3). Section I takes cylinder diameter and kinematic viscosity into account, and plots equation (11) as a family of lines converting shedding frequency to velocity. Section II converts velocity to $(\text{velocity})^{0.45}$. Section III takes the wire cold resistance R_a and the current I into account, and converts the hot wire voltage to a form which is linear with $(\text{velocity})^{0.45}$ (Equation (10)). The calibration points can now be plotted directly on Section IV as the data is taken. The use of this system allows an accurate calibration curve to be plotted in less than ten minutes. By varying cylinder size, it is possible to get accurate values of velocity from 15 cm sec^{-1} to well over 500 cm sec^{-1}. Care must be taken, however, to insure that the finite dimensions of the test

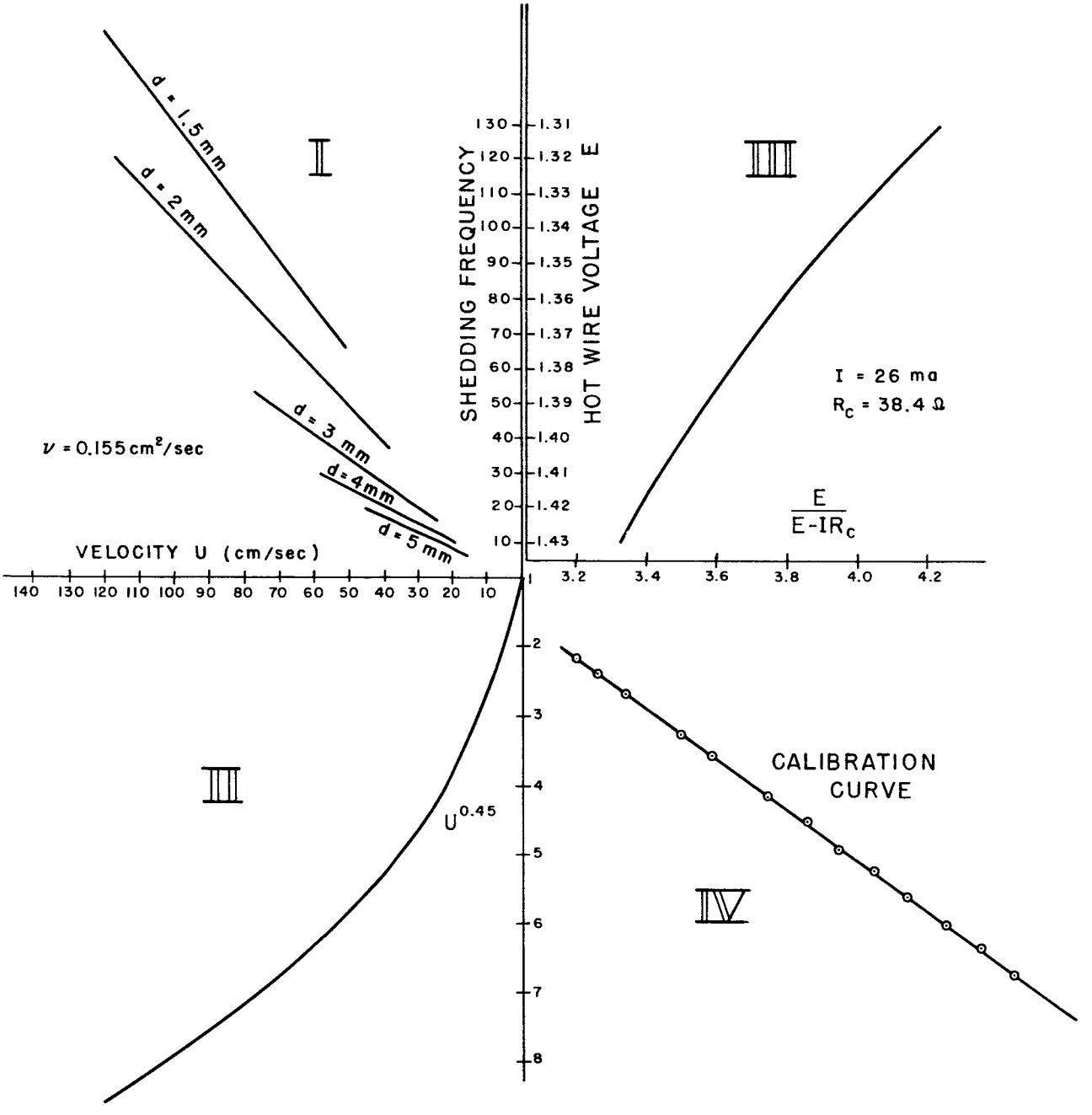

Figure A.3 The multi-element calibration curve used for hot wire calibration

them, and pressed tightly against them. Heat is then applied to each needle in turn, well down away from the wire, until the solder flows and forms a smooth joint. Care must be exercised at this point to apply no more heat than is necessary for the solder, since the etched wire burns through quite easily. After both joints are soldered, the ends of the wire may be broken off with fine tweezers, and the probe is ready for calibration.

The second method is to solder the unetched wire to the needles, and then etch a portion of the wire between the supports. This method has an advantage in that it allows the use of shorter sensing wire lengths than the previous method. The unetched wire is of sufficient size that it may conveniently be soldered to the probe by hand without the need for manipulators or optical devices. The center portion of the mounted wire is then etched by allowing acid from a fine tube to drip slowly over the wire. The diameter of the drip tube determines the length of the etched portion. The resistance of the wire can be monitored with an ohm meter during this process, and two or more wires can be made to have equal sensitivity by adjusting the etched length. When the etching process is complete, the acid should be neutralized and the wire washed in clean water. It is now ready for calibration.

A.4 Hot Wire Calibration

The relationship between wire resistance and velocity of flow past the wire was developed earlier as:

$$\frac{I^2R}{R - R_a} = A + BU^{0.45}$$

where A and B were constants for a constant overheat ratio. For constant current operation, the overheat ratio does not remain constant, but the fluctuations are small enough that A and B may safely be considered as constants.

The uncompensated constant current anemometer in its simplest form consists of a power supply, a large resistance, and the hot wire; all in series so that the current through the wire is effectively independent of its resistance. The voltage across the wire then varies as a linear function of the resistance, which is a non-linear function of the velocity. The response of the uncompensated wire shows no attenuation of amplitude with frequency up to frequencies of several hundred cps (Flow Corporation [22]); and a compensating amplifier was not necessary in these experiments.

To obtain known velocities, a small wind tunnel (figure A.2) was built which allowed the entire hot wire traversing mechanism to be mounted on the test section. Upstream in the test section a small hole was drilled in the side to allow the insertion of various sized cylinders across the flow. The vortices shed by these cylinders above a certain rod Reynolds number ($Re_r = Ud/\nu$) appear as a sinusoidally varying voltage in the hot wire. Following Roshko [16], the relationship between velocity and Strouhal shedding frequency is taken as:

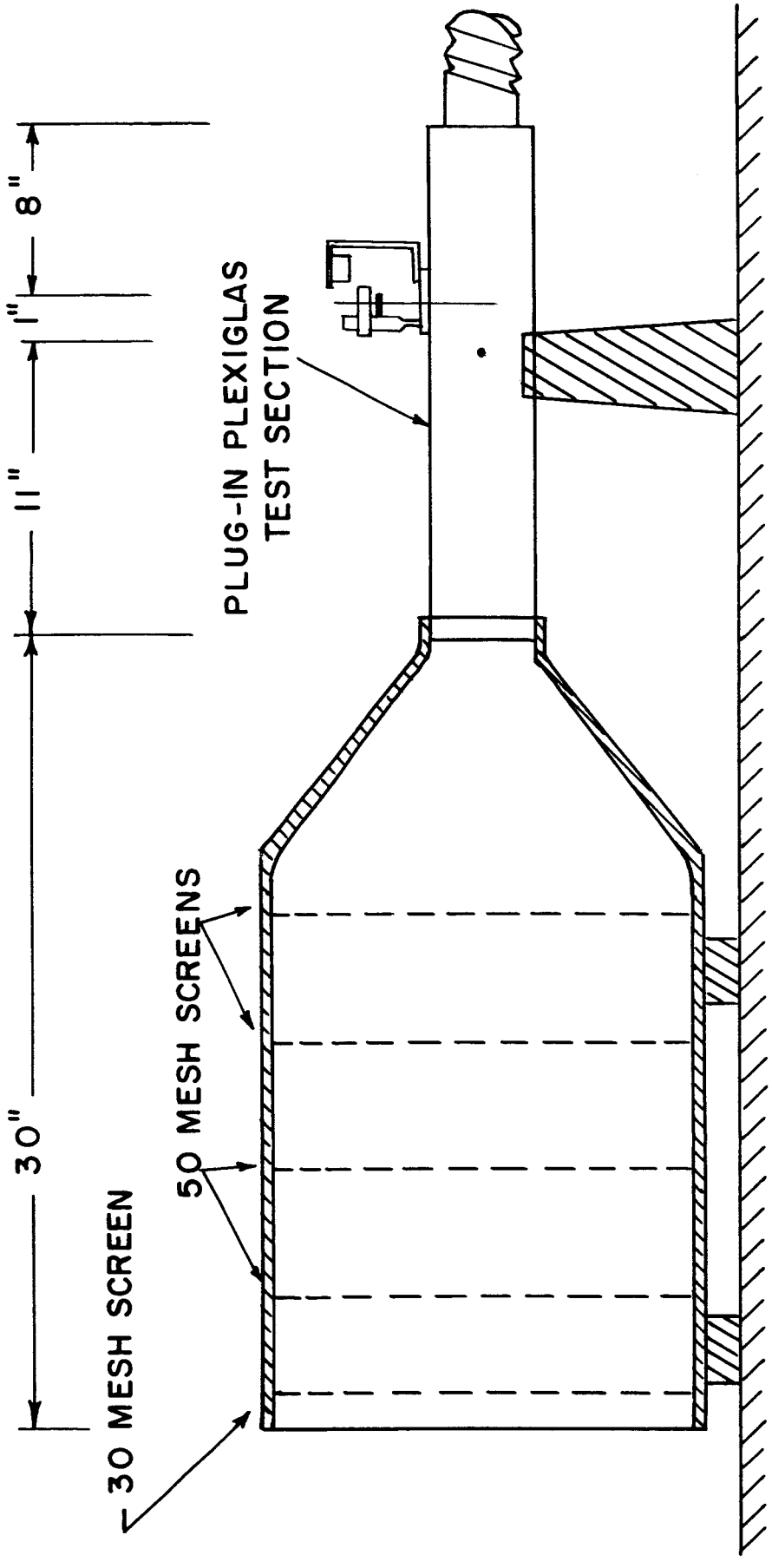

Figure A.2 Schematic diagram of the wind tunnel used for hot wire calibration

section in use do not influence the shedding frequency. This is easily checked by using more than one cylinder at the same velocity to see if they yield the same results; and in general can be avoided by operating at the lowest possible rod Reynolds number. With the calibration curve plotted, the graph is a useful working tool which converts hot wire voltages directly to velocities.

A.5 Hot Wire Operation

Probably the biggest single factor in the successful use of hot wire anemometers is the exercise of reasonable care in handling them. There is nothing quite so frustrating as breaking a wire after having spent hours in building and calibrating it. When not in use, the probes should be shock mounted and stored in a closed container.

The actual operation of the anemometer consists of nothing more than setting the desired value of current, based on the desired overheat ratio, and then monitoring the output voltage by some convenient means. Plotters and recorders have the advantage of creating a permanent record, but they may introduce some distortion to the signal due to their own system dynamics. Oscilloscope photographs seem to offer the least distorted picture of the output.

Since the wire is primarily sensitive to flow at right angles to it, it may be used to determine the direction as well as the magnitude of the flow. This technique is described in III.1.